Development of an actuator disk model for large eddy simulations of the Helix wind farm control approach

by

S.I.H. Sekha

Student Name	Student Number
Swen Sekha	4665325

Supervisor:	R.A. Verzijlbergh
Assessment committee:	R.A. Verzijlbergh, S. Kenjereš, J.W. van Wingerden, E. Taschner
Project Duration:	09/2023 - 05/2024
Faculty:	Faculty of Applied Physics, Delft

TU Delft

Acknowledgements

I am deeply grateful to everyone who supported me throughout this project.

In particular, I would like to thank Remco for his supervision and the insightful weekly discussions at the Whiffle office. The weekly meetings provided new insights and his guidance ensured I stayed focused on the project's research goals.

Special thanks to Emanuel and Jonas for their supervision and incredible enthusiasm for the project. After each weekly meeting with really valuable discussions, where running out of time was the only issue, I always left energized and full of new ideas.

Additionally, I would like to thank my fellow thesis student Diederik for his cooperation throughout the project and the insightful and fun discussions we have had.

Finally, I extend my appreciation to all Whiffle employees who have helped me along the way, with a special thanks to Pim, Gerben and Mikko.

Abstract

The Helix approach is a dynamic control method that mitigates wind turbine wake effects by pitching the turbine blades individually. In current literature the method is mainly researched with a high-fidelity actuator line model (ALM). Because of the computational constraints imposed by this model, the effect of the Helix has not been researched for turbine arrays longer than 3. To investigate the effects of the Helix on a farm size scale, a lower fidelity model capturing the Helix is developed in this research. This model is based on a uniform actuator disk model and is called the H-ADM. The H-ADM is validated in laminar conditions at a fine resolution by comparing wake recovery to the ALM. The H-ADM captures both the additional wake mixing and wake displacement caused by the Helix. Furthermore, the H-ADM correctly predicts differences between the counterclockwise (CCW) and clockwise (CW) Helix. Due to modelling assumptions, the H-ADM can run simulations at a coarser resolution and with a smaller time-step than the ALM. Computational gains are achieved with the H-ADM as a result. This research shows that similar simulations are executed over 640 times faster for the H-ADM compared to ALM. The model is used to gain a deeper understanding of the mechanisms causing differences between the CCW and CW Helix. It turns out these differences fade away if no rotational force is exerted by the wind turbine. Finally, the computational gains of the H-ADM are leveraged by applying the Helix on the first row of a large scale wind farm with 48 turbines. For the considered farm the CCW Helix seems to outperform the CW Helix in terms of total power gains.

Contents

1 Introduction

In June 2023 the globally installed wind power capacity equalled 976 GW (WWEA, 2023). Operating at maximum capacity, this equals nearly double the United States' electricity consumption in 2022 (IEA, 2022). It is expected that by 2027, this capacity will increase by an additional 680 GW (GWEC, 2023). Clustering these wind turbines into farms has many advantages. It enhances land use efficiency by generating more power in a smaller area and facilitates energy transmission efficiency minimizing energy losses. Also, constructing multiple turbines simultaneously utilizes economies of scale, reducing the cost per unit of energy produced. However, clustering wind turbines also has disadvantages. The turbines in the front of the cluster can decrease the wind speed available to those behind them, thereby reducing the overall energy output. Over the past few year, the scientific interest in understanding and increasing wind farm efficiency has risen.

1.1. Wind farm dynamics

Wind turbines generate electricity by rotating. This rotating motion is caused by the wind exerting a force on the turbine blades with a component in the rotor plane. This force also has a component parallel to the rotor axis pushing the turbine back. Following Newton's third law, the turbine exerts forces equal in magnitude but opposite in direction on the airflow. This decreases the kinetic energy and increases the turbulence of the flow within a volume downstream of the wind turbine. This disturbed region is called the wake region (Vermeer et al., 2003). These effects induce a reduced power production of wind turbines positioned within a turbine wake (Barthelmie et al., 2010; Hansen et al., 2012). Next to that, the higher turbulence levels can reduce the turbine life time due to increased fatigue loads (Thomsen & Sørensen, 1999). A visualization of a wind turbine wake and its effect on a turbine positioned in the wake is shown in figure 1.1a.

Studies focusing on wakes behind individual wind turbines can be split into those where the inflow is laminar and those where the inflow is turbulent (Stevens & Meneveau, 2017). The former is suited for evaluating wind turbine representations in models, while the latter offers a more accurate depiction of the conditions found in the Atmospheric Boundary Layer (ABL). With laminar inflow the turbine wake is expected to grow far downstream following a 1/3 power law (Larsen, 1988; Tennekes & Lumley, 1972). This scaling law assumes that turbulent wake eddies predominantly drive local turbulent transport. However, in the ABL mixing is dominated by ABL eddy structures that accelerate the wake recovery.

Wake recovery can also be accelerated by wind turbine control. Not only can wind turbine control in this way result in power gains, it can also help reduce turbine loads (Andersson et al., 2021; Novaes Menezes et al., 2018). These control methods can be split into quasi-static and dynamic methods (Meyers et al., 2022). Quasi-static methods adjust turbine settings at a slow rate, aligning them with general meteorological changes. In contrast, dynamic methods seek to incorporate more immediate flow dynamics and can even directly manipulate wake mixing. For both methods, two different approaches can be distinguished: induction control and wake steering. Induction control reduces the induction of upstream turbines, leaving more energy in the flow for downstream turbines (Nilsson et al., 2015). Wake steering methods redirect the wake of upstream turbines decreasing the overlap with downstream turbines. Kheirabadi and Nagamune (2019) have found that wake steering methods yield more consistent

power gains, whereas axial induction control has higher potential for load reduction.

Focusing on dynamic methods, Munters and Meyers (2016) have researched dynamic induction control (DIC). Here the induction of the first-row turbines is controlled by a sinusoidal signal, creating a pulsing motion in the wake. Kimura et al. (2019) have simulated the effect of dynamic wake steering, where the turbine yaw angle varies sinusoidally. Both dynamic control methods have shown promising results by accelerating the recovery of velocity deficits in the wake region. However, due to the varying induction factor or yaw angle, the turbine power and loads vary rapidly.

1.2. Helix control method

Frederik et al. (2020) proposed a new dynamic control strategy called the Helix. The Helix is a form of dynamic individual pitch control (DIPC). The method induces sinusoidal variations of the tilt and yaw moments exerted upon the rotor by individual blade pitching. As a result, the resultant force on the rotor is displaced from the center and rotates around. This induces a helical pattern in the wake, hence the name Helix. The Helix wake effect is visualized in Figure 1.1b. An advantage of this DIPC method is that it produces relatively low power and thrust variations, alleviating periodic loads on the turbines.

Frederik et al. (2020) have studied both the counter-clockwise (CCW) and clockwise (CW) rotation of the Helix up to a distance of 7 rotor diameters behind the Helix turbine. On this domain the CCW orientation showed the quickest wake recovery. In a two-turbine wind farm the CCW Helix can increase the power production by 7.5% for a Helix amplitude of 4°. The actuation signal used was based on an optimal Strouhal number (St) of 0.25 as suggested by other dynamic induction control (DIC) studies. However, recent research has shown that the ideal St number for the Helix might deviate from 0.25 (Muscari et al., 2022). Furthermore, Taschner et al. (2023) have researched the optimal pitch amplitude for the Helix approach. Here no saturation of the power gain was detected for pitch amplitudes up to 6° in low turbulence conditions. Therefore, setting the Helix amplitude will be a trade-off between power gains and increased loads on the tower and blades. This trade-off has also been identified in other studies that looked at the increased loads on Helix turbines (Frederik & van Wingerden, 2022; Vondelen et al., 2023).

A closer understanding of processes in the helical wake is researched by Korb et al. (2023). They found that the power gains of the Helix approach are a result of both the deflection of the wake and increased mixing of ambient air. Both effects are more beneficial in low turbulence conditions. Wind tunnel experiments investigating the Helix by van der Hoek et al. (2023) showed that the breakdown

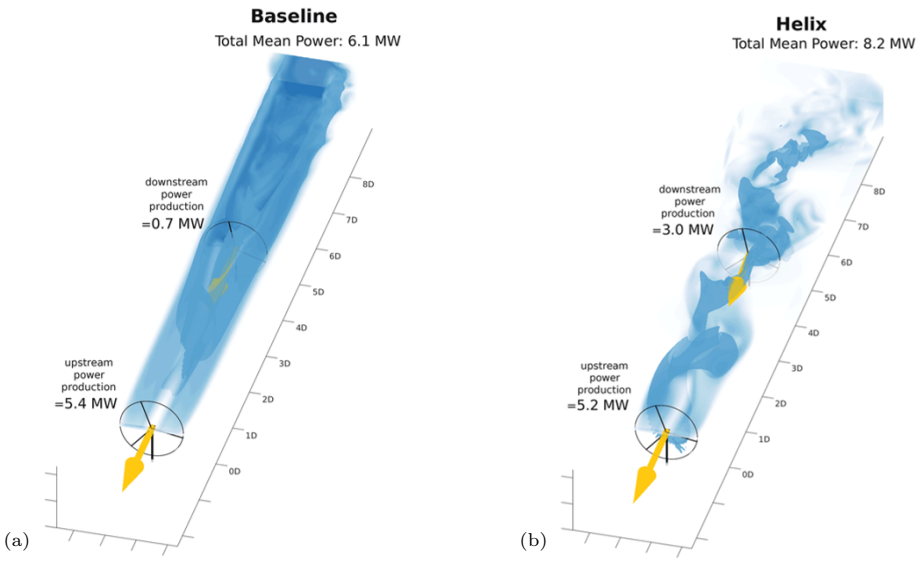

Figure 1.1: LES results in laminar inflow of wind turbine wakes along downstream distances. The downstream distance is normalized by the turbine diameter (D). Dark blue shading corresponds to an isosurface of the velocity; light blue shading in the horizontal plane corresponds to the velocity magnitude. Subfigure (a) provides a visualization of a wind turbine wake in normal operating conditions and (b) of a wind turbine operating with the Helix control method. Figure from Meyers et al. (2022).

of tip vortices is enhanced with the Helix approach. This earlier breakdown of tip vortices is known to cause an earlier recovery of the wake velocity (Lignarolo et al., 2014). These wind tunnel experiments were also able to verify that the CCW configuration leads to a quicker wake recovery than the CW configuration within the studied region of the wake.

1.3. Turbine modelling

Most of the computational research investigating the Helix approach uses an Actuator Line Model (ALM) to simulate the interaction between the turbine and surrounding flow (Sørensen & Shen, 2002). The surrounding flow is resolved using large eddy simulations (LES). The ALM simulates individual turbine blades by splitting them in multiple elements. For each element the lift and drag force is calculated using airfoil look-up tables. The ALM is able to capture detailed physics of a wind turbine wake, such as tip vortices and periodic helicoidal vortices (Ivanell et al., 2009; Troldborg et al., 2007). However, the ALM requires a fine grid resolution and a small time step that is restricted by the tip speed, resulting in relatively high computation times (Martínez et al., 2012).

A lower fidelity model that can be used to simulate wind turbine aerodynamics is called the Actuator Disk Model (ADM). Here the rotor swept area is divided into many elements, without resolving the individual blades (Jimenez et al., 2007). This relaxes time constraints for the ADM compared to the ALM. One type of ADM uses blade element (BE) theory to calculate the forces exerted by the disk (Wu & Porté-Agel, 2011). This type of ADM, the BE-ADM, still relies on airfoil look-up tables. Another type of ADM is based on a uniform distribution of thrust and rotational force over the disk area (Calaf et al., 2010; Meyers & Meneveau, 2010). Here the total thrust and rotational force exerted by the disk are calculated using turbine look-up tables.

To simulate the effect of the Helix approach on larger scale, the time and resolution constraints of the ALM are prohibitive. For this reason, the Helix has not been simulated for an array of turbines larger than three (Korb et al., 2023). One way to allow for larger scale Helix simulations would be the development of an ADM that can capture the effects of the Helix approach. Coquelet et al. (2023) have done this using the BE-ADM framework. They were able to capture the forced motion of the wake and the faster wake recovery of the CCW helix, for a coarse resolution of 16 gridpoints per turbine diameter. However, the Helix BE-ADM was not able to capture the different wake recovery of the CCW and CW configurations.

1.4. Research objective and outline

This research aims to address the following three gaps in literature: (i) Developing and validating a Helix ADM without requiring airfoil look-up tables. For most wind turbines this specific blade design information is classified, making it difficult to apply the model universally to different turbines (Simisiroglou et al., 2017). (ii) Using the developed Helix ADM to gain a better understanding of the phenomenology underlying the difference between the CW and CCW Helix. (iii) Applying the Helix ADM on a farm-size scale to assess the downstream effects of upstream Helix actuation. All simulations in this research model the IEA 15MW reference turbine defined by Gaertner et al. (2020).

The report is organized as follows. Chapter 2 describes LES and the ADM implementation. In Chapter 3 the most important theory of the Helix approach is explained and the Helix ADM is developed, focusing on the first part of research goal (i). Then, Chapter 4 completes research goal (i) by verifying and validating the developed Helix ADM. In Chapter 5 the Helix ADM will be applied to research the differences between CW and CCW, thereby realizing research goal (ii). Chapter 6 addresses research goal (iii) by applying the Helix ADM to a farm size simulation. Finally, Chapter 7 discusses the key results of this report and Chapter 8 makes suggestions for future research.

2

Model Description

This research utilizes the GPU-Resident Atmospheric Simulation Platform (GRASP), an LES solver provided by Whiffle. GRASP is described in Section 2.1. Section 2.2 discusses actuator disk theory and modelling. Finally, the implementation is discussed in Section 2.3.

2.1. GRASP

The foundational framework of GRASP originates from the Dutch Atmospheric Large Eddy Simulation (DALES) model (Heus et al., 2010). Both LES models solve the filtered three-dimensional Navier-Stokes equations. The spatial filtering separates the large-scale motions from the small-scale motions. The large scale motions are resolved, whereas the smaller scales are modelled using a subgrid-scale (SGS) model. In order to boost computational performance, the DALES model has been adapted to run on GPUs in stead of CPUs (Schalkwijk et al., 2015). Similarly, GRASP uses GPUs to solve the Navier-Stokes equations and allow for parallelization. The GRASP model diverges from the original DALES structure in incorporating an anelastic approximation (Böing et al., 2012). The filtered equations for mass and momentum are now given by:

$$\frac{\partial \rho_b \tilde{u}_j}{\partial x_j} = 0 \tag{2.1}$$

$$\rho_b \frac{\partial \tilde{u}_i}{\partial t} + \frac{\partial \rho_b \tilde{u}_i \tilde{u}_j}{\partial x_j} = -\frac{\partial p}{\partial x_i} + \rho_b b \delta_{iz} + \frac{\partial \tau_{ij}}{\partial x_j} + \varepsilon_{ijz} f_c (\tilde{u}_j - u_j^g) + f_i^{WT} + f_i^{Fringe} \tag{2.2}$$

with $i \in \{x,y,z\}$, $\tilde{u}$ the filtered velocity, $\rho_b = \rho_b(z)$ the reference density according to the anelastic approximation, p the pressure, b a representation of the buoyancy term, τ_{ij} the subgrid-stress tensor, f_c the Coriolis parameter, u^g the geostrophic wind, f^{WT} the wind turbine body force and f^{Fringe} an external force that can be used to for example nudge the flow. This research uses a Cartesian coordinate system where (x, y, z) correspond to the streamwise, lateral and vertical direction respectively. The velocity components (u_x, u_y, u_z) will be denoted by (u, v, w). In the remainder of this report the tilde will be dropped for sake of convenience.

2.1.1. Boundary conditions

Simulations are set up using periodic boundary conditions for all sides of the domain. To ensure that disturbed airflow of a turbine wake does not re-enter the domain, the flow is nudged towards a reference simulation using f^{Fringe} of Equation 2.2 (Stevens et al. (2014), Munters et al. (2016)). This reference simulation is run with similar domain settings but does not contain momentum sinks (e.g. a wind turbine). Therefore, nudging the turbine simulation towards the reference simulation allows for periodic boundary conditions without wake re-entering:

$$f_i^{Fringe} = -\rho_b \frac{\kappa(x,y,z)\eta}{\Delta t} (\zeta_i - \zeta_i^{ref}) \tag{2.3}$$

Here, κ is a spatial factor equal to 1 at the edges of the domain, and decaying to 0 at a distance L_n from the edges following a second-order polynomial. The nudge strength is controlled by η and Δt is the

simulation time step. Finally, ζ denotes the simulation variable that is being nudged, e.g. the velocity component u. The superscript 'ref' corresponds to the reference simulation.

For the top of the domain, the following boundary conditions are used:

$$\begin{aligned} \frac{\partial u}{\partial z} = \frac{\partial v}{\partial z} &= 0 \\ w &= 0 \end{aligned} \tag{2.4}$$

Given GRASP's limitations in handling zero-shear-stress bottom boundaries, a near-zero friction velocity u^* is configured to suppress the formation of a boundary layer.

2.2. Uniform actuator disk

Actuator disk theory can be used to simulate the interaction between a wind turbine and airflow. The theory treats the rotating blades of the wind turbine as a thin disk that acts as an actuator, exerting forces on the air passing through it. Following this theory, wind turbines can be simulated with LES as a set of local momentum sinks distributed across the rotor disk area, effectively simulating the turbine without resolving individual blades (Jimenez et al., 2007). The fact that the turbine blades do not need to be resolved relaxes the constraints on the simulation timestep (Martínez et al., 2012). This means that simulations using an actuator disk model can be much faster than simulations that resolve the individual blades, such as the ALM.

2.2.1. Actuator disk theory

The actuator disk model is derived from axial momentum theory that applies conservation laws to a stream-tube containing the wind turbine, see Figure 2.1 (Burton et al., 2001; Manwell et al., 2010). For each streamwise location, the static pressure p and velocity u differs. The increase in static pressure as the flow reaches the actuator disk causes the axial free stream velocity u_∞ to reduce. At the actuator disk surface the flow has slowed down to the axial disk velocity u_d. The ratio between u_∞ and u_d is defined as the axial induction factor $a = (u_\infty - u_d)/u_\infty$. The disk causes a sudden drop in static pressure level. After the disk, the static pressure is below atmospheric pressure and increases again. This causes the wind velocity to slow down further creating a wake with velocity u_w behind the wind turbine. By applying conservation laws of momentum, mass and energy (Bernoulli) the following relation between the free stream velocity and wake velocity can be found

$$u_w = (1-2a)u_\infty \tag{2.5}$$

This important result shows that half of the total induction takes place before the actuator disk, and the other half behind the actuator disk. Plugging the equations for the velocities in the thrust and power equation, we can express them in terms of the axial induction factor. This yields the following relation between the coefficient of thrust C_T, coefficient of power C_P and a:

$$C_T = 4a(1-a) \tag{2.6}$$

$$C_P = 4a(1-a)^2 \tag{2.7}$$

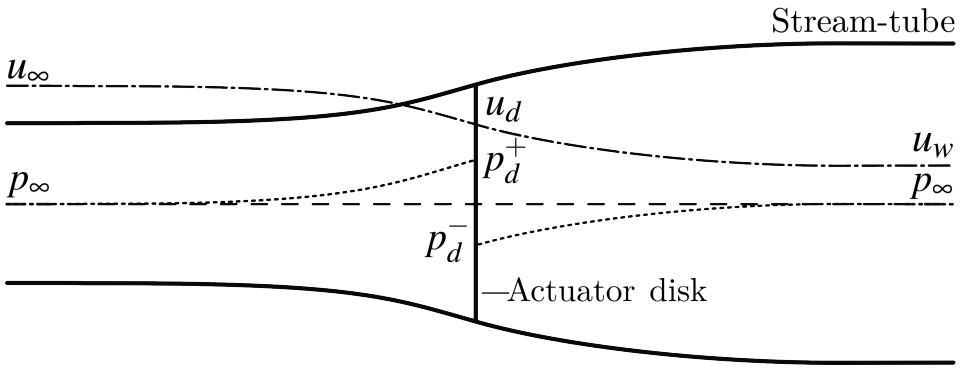

Figure 2.1: Visualization of the stream-tube with an actuator disk inside it. Adapted figure from Burton et al. (2001).

Extending this concept, we can include wake rotation via angular momentum. Similar to the axial induction factor, a tangential induction factor a' can be defined as $a' = \omega/2\Omega$. Here ω denotes the angular velocity of the wake and Ω the angular velocity of the turbine rotor. The axial induction is related to the tangential induction through the local speed ratio $\lambda_r = \Omega r/u_\infty$:

$$a' = a(1-a)/\lambda_r^2 \tag{2.8}$$

2.2.2. Uniform actuator disk

Actuator disk theory learns us that the rotor area can be approximated by a disk surface. This can be implemented in LES to simulate the effect of wind turbine forces with different inflow conditions. Following Meyers and Meneveau (2010) and Calaf et al. (2010), the total thrust force $F_{n,disk}$ and rotational force $F_{\theta,disk}$ exerted by the rotor disk on the LES grid can be calculated by

$$F_{n,disk} = \frac{1}{2}\rho C_T \pi R^2 u_\infty^2 \tag{2.9}$$

$$F_{\theta,disk} = \rho C_P \pi R \frac{u_\infty^3}{\Omega} \tag{2.10}$$

with R the turbine radius. Applying these forces directly to the LES grid by uniformly distributing them over the rotor disk area can lead to steep velocity gradients and numerical instabilities. Instead, forces are distributed using a Gaussian convolution over LES grid cells (Wu & Porté-Agel, 2011). The location of such an LES grid cell is denoted by a vector $\mathbf{x}$ and the rotor plane is given by coordinates $\mathbf{x_t}$, with $\mathbf{x}_0$ the coordinates of the rotor center. Now, $\mathbf{e}_n \cdot (\mathbf{x}_t - \mathbf{x}_0) = 0$ with $\mathbf{e}_n$ the unit vector perpendicular to the rotor plane. Furthermore, we have a polar coordinate system in the turbine rotor plane with vectors $\mathbf{y}$. The origin of this system is located in the rotor center and a coordinate transformation $\mathbf{y}(\mathbf{x}_t - \mathbf{x}_0)$ allows to map the local rotor plane coordinates to the corresponding LES coordinates. Now, the Gaussian convolution is given by (Calaf et al., 2010; Meyers & Meneveau, 2010):

$$\mathscr{R}(\mathbf{x}) = \iiint S(\mathbf{x}')G(\mathbf{x}-\mathbf{x}')\delta(\mathbf{e}_n \cdot (\mathbf{x}' - \mathbf{x}_0))H(R - \|\mathbf{y}(\mathbf{x}' - \mathbf{x}_0)\|)\, d^3\mathbf{x}' \tag{2.11}$$

The product between the delta δ and heaviside function H is only nonzero when $\mathbf{x}'$ is on the actuator disk, i.e. only virtual points on the actuator disk have a Gaussian contribution. Those points are defined on a polar grid following Réthoré et al. (2014), where they are spaced apart by a constant interval in radial and tangential direction, dr and dt respectively. A visualization can be found in Figure 2.2. The result is that actuator disk points represent different fractions of the total disk area. To account for this, the solidity factor $S(\mathbf{x})$ is defined. The solidity expresses the area of each actuator disk point $r(\mathbf{x})drdt$ as a fraction of the total disk area. The Gaussian kernel G is defined as:

$$G(x) = \left(\frac{6}{\pi\varepsilon^2}\right)^{\frac{3}{2}} \exp\left(-6\frac{\|x\|^2}{\varepsilon^2}\right) \tag{2.12}$$

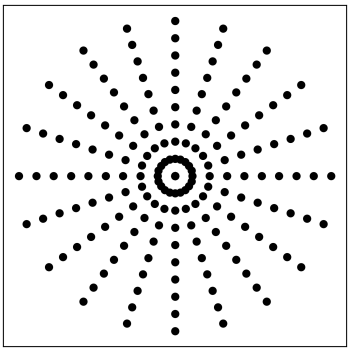

Figure 2.2: Actuator disk points defined on a polar grid. The interval in radial and tangential direction is constant for all points, resulting in points representing different fractions of the total disk area.

with $\varepsilon = \alpha\Delta_{grid}$. Here Δ_{grid} denotes the LES gridsize. In this study the gridsize is equal in streamwise, lateral and vertical direction. Since the simulation approximates the actuator disk surface by discrete actuator disk points, Equation 2.11 is converted to a summation. In order to conserve normalization of the convolution kernel, the summation should be normalized (van Dorp, 2016):

$$\mathscr{R}^N(\mathbf{x}) = \frac{\mathscr{R}(\mathbf{x})}{\sum_\chi \mathscr{R}(\chi)} \tag{2.13}$$

where the set χ contains all $\mathbf{x}$ with $\mathscr{R}(\mathbf{x}) \neq 0$. Figure 2.3 depicts the normalized Gaussian convolution for a turbine diameter $D = 15\Delta_{grid}$ and $\alpha = 2$. Now, according to a uniform actuator disk (U-ADM) the wind turbine body force of Equation 2.2 can be calculated as:

$$\mathbf{f}^{WT}(\mathbf{x}) = \frac{\mathscr{R}^N(\mathbf{x})}{v(\mathbf{x})}\left(F_{n,disk}\mathbf{e}_n + F_{\theta,disk}\mathbf{e}_\theta(\theta_0(\mathbf{x}),\Omega)\right) \tag{2.14}$$

with v the gridcell volume, $\mathbf{e}_\theta$ the azimuthal unit vector in the rotor plane and θ_0 the azimuthal position in the rotor plane.

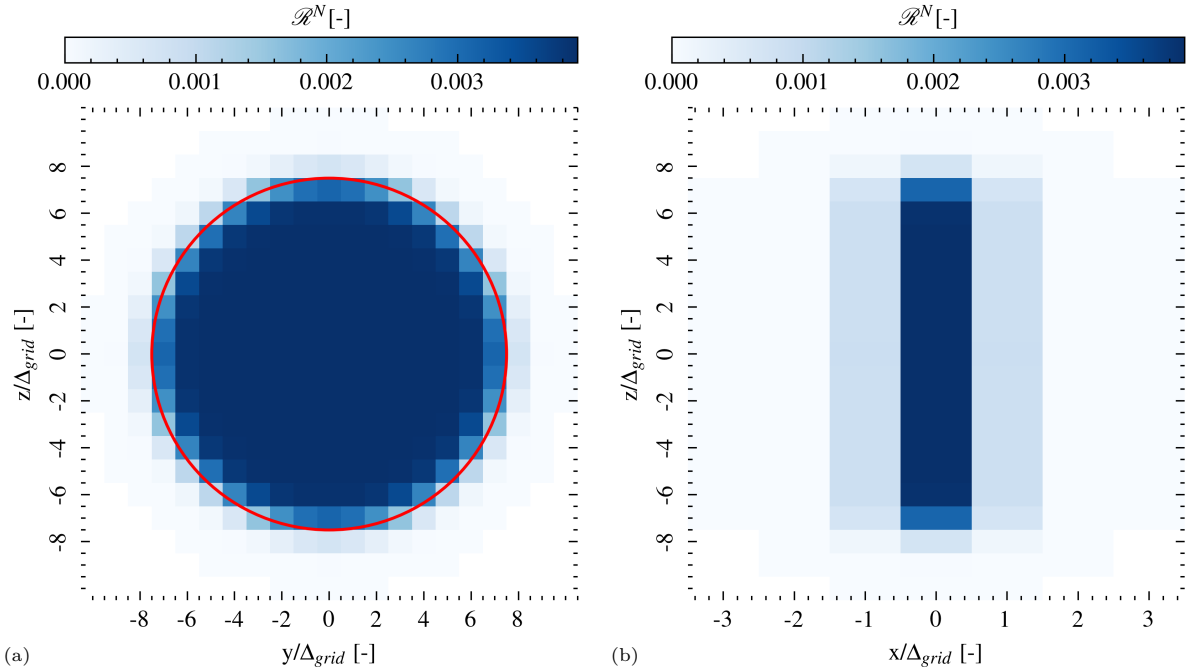

Figure 2.3: Cross sectional view of the normalized Gaussian projection kernel $\mathscr{R}^N$. The disk is oriented perpendicular to streamwise direction and the center is located at x = y = z = 0. (a) provides a cross section in streamwise direction where the red circle indicates the rotor area. (b) provides a cross section in lateral direction, showing that the Gaussian convolution smears the effect of the 2D disk over a 3D volume.

2.3. A note on the free stream velocity

So far, computations involving the free stream velocity u_∞ have been the primary focus. When simulating one turbine this free stream velocity is known and the provided equations can be used (Stevens et al., 2018). However, when multiple turbines are present in the simulation domain, it is impossible to determine an unperturbed upstream velocity since upstream values are affected by other turbines. In this case it is most convenient to use the axial velocity at the rotor disk. This requires a new thrust and power curve, C_T' and C_P' respectively, that expresses C_T and C_P in terms of the disk velocity (Simisiroglou et al., 2017). There are different ways to do this, but in this research a routine developed by Whiffle is used (Baas et al., 2022). The thrust and azimuthal force equations, originally presented as Equations

2.9 and 2.10, can now be rewritten to (Meyers & Meneveau, 2010):

$$F_{n,disk} = \frac{1}{2}\rho C_T' \pi R^2 \bar{u}_d^2 \tag{2.15}$$

$$F_{\theta,disk} = \rho C_P' \pi R \bar{u}_d^2 \frac{u_d}{\Omega} \tag{2.16}$$

with u_d the axial disk averaged velocity and $\bar{u}_d$ its time averaged value using a one sided exponential filter (van Dorp, 2016). The IEA 15MW rotational speed varies between 5.0 and 7.6 rpm. Therefore, the exponential filter smoothing time scale T is chosen to match the average rotational speed of 6.3 rpm; $T = 60/6.3 = 9.5s$. The axial disk averaged velocity is calculated using:

$$u_d = \iiint \mathscr{R}^N(\mathbf{x})\mathbf{M}(\mathbf{x}) \cdot \mathbf{e}_n \, d^3\mathbf{x} \tag{2.17}$$

with $\mathbf{M}(\mathbf{x}) = [u(\mathbf{x}), v(\mathbf{x}), w(\mathbf{x})]$.

3

Helix actuator disk

The goal of this chapter is to derive the Helix ADM. First, Section 3.1 introduces relevant theory of the Helix control method and discusses the requirements of this new actuator disk. Then, Section 3.2 and 3.3 derive the Helix ADM.

3.1. Helix control method

The Helix is a dynamic individual pitch control (DIPC) method introduced by Frederik et al. (2020). The method induces sinusoidal variations of the tilt and yaw moments exerted upon the rotor. As a result, the rotor force vector is displaced from the center and rotates around. This causes the wake to continuously change direction and shape compared to a baseline wake. The multiblade coordinate (MBC) transformation shows that the momentum variations can be achieved by adjusting the individual blade pitch angle β_b for the three blades $b \in \{1,2,3\}$ (Bir (2008)):

$$\begin{bmatrix} \beta_1(t) \\ \beta_2(t) \\ \beta_3(t) \end{bmatrix} = \begin{bmatrix} \cos(\theta_1(t)) & \sin(\theta_1(t)) \\ \cos(\theta_2(t)) & \sin(\theta_2(t)) \\ \cos(\theta_3(t)) & \sin(\theta_3(t)) \end{bmatrix} \begin{bmatrix} \beta_t(t) \\ \beta_y(t) \end{bmatrix} \tag{3.1}$$

here β_t and β_y denote the rotor tilt and yaw angle, respectively, and θ_b the azimuthal position of the three blades in the rotor plane. The excitation frequency f_e of β_t and β_y is characterized by the dimensionless Strouhal number St:

$$St = \frac{f_e D}{u_\infty} \tag{3.2}$$

Now, imposing the excitation frequency on the yaw and tilt angle of the rotor will cause a rotation over time (Coquelet et al., 2023):

$$\beta_t(t) = A\sin(2\pi f_e t) \quad \text{and} \quad \beta_y(t) = A\cos(2\pi f_e t) \tag{3.3}$$

$$\beta_t(t) = A\sin(2\pi f_e t) \quad \text{and} \quad \beta_y(t) = -A\cos(2\pi f_e t) \tag{3.4}$$

with A the helix amplitude. Equation 3.3 corresponds to a counterclockwise (CCW) rotation of the wake and Equation 3.4 to a clockwise (CW) rotation. Finally, the required individual blade pitch angles can be calculated using Equation 3.1 (Frederik et al., 2020):

$$\beta_b(t) = \pm A\sin(\theta_{0,b} + 2\pi(f_r \pm f_e)t) \tag{3.5}$$

with $\theta_{0,b}$ the azimuthal position of blade b at time $t = 0$ and f_r the rotational frequency of the wind turbine blades. Here, and in the remainder of this report, the '+' corresponds to a CCW Helix and the '-' to a CW Helix. This sequence of Helix control operations leading to the varying tilt and yaw moments M_t and M_y is visualized in Figure 3.1.

From Equation 3.5 it follows that, at a certain time t, the three blade pitch angles are different based on their initial azimuthal position. Consequently, the forces exerted by each blade differs as well. The Helix actuator disk (H-ADM) should capture this distinct blade effect. However, fundamentally an actuator disk does not capture individual blade behaviour, but rather rotor averaged effects. The remainder of this chapter discusses how the classic ADM is adapted in order to capture these effects of the Helix approach.

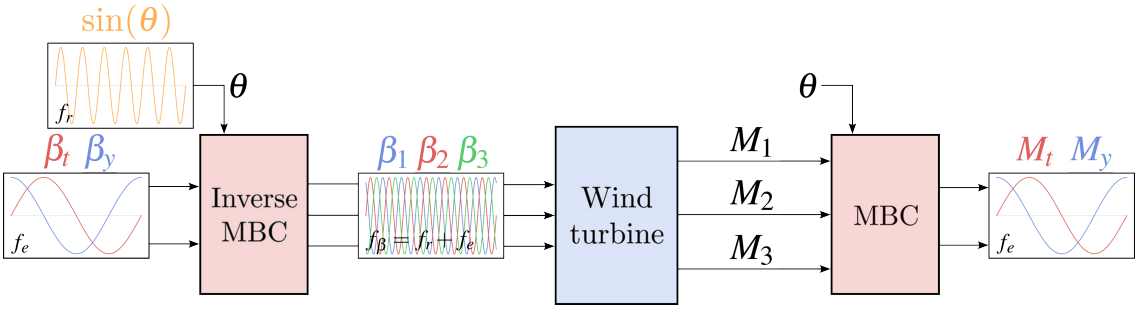

Figure 3.1: A representation of how the MBC transformation is used to achieve periodic yaw and tilt moments on the turbine. Adapted figure from Frederik et al. (2020).

3.2. Azimuthal force distribution

As said, the individual blade pitch behaviour of the Helix approach causes the forces of the three turbine blades to vary mutually. As a result, the blade forces are distributed non-uniformly in azimuthal direction over the rotor disk area. To achieve this asymmetry of forces over the disk, the U-ADM is extended by introducing a new projection kernel. This new projection kernel is called the Helix projection kernel (HPK). In order to derive the HPK, the azimuthal force distribution of a Helix with $St = 0$ will be derived. For $St = 0$ the blade pitch frequency is equal to the rotor rotational frequency. This means that the pitch signal is periodic with 2π as a function of azimuth. As a result, exactly one pitching period can be captured by the disk surface. A non-zero Strouhal Helix is then modelled by rotating the zero Strouhal distribution with the corresponding excitation frequency.

3.2.1. Stationary distribution

To derive the stationary distribution, i.e. $St = 0$, blade element theory is used (Burton et al., 2001). Here each rotor blade is split into e blade elements i, see Figure 3.2. The flow angle ϕ_i is defined as $\phi_i = \tan^{-1}(\frac{u_i}{\Omega r_i})$ with u_i the axial wind velocity at element i. It is assumed that the incoming flow is perpendicular to the rotor disk, i.e. u_i is the only wind velocity component. The angle of attack is defined as $\alpha_i = \phi_i - \beta_b - \gamma_i$ with γ_i the twist angle of the blade element. For each blade element the lift and drag force, $F_{L,i}$ and $F_{D,i}$ respectively, can be calculated. By summing the calculated forces over all blade elements and blades, the total disk forces of Equations 2.9 and 2.10 can be found. Assuming $F_{L,i} >> F_{D,i}$ results in:

$$\begin{aligned} F_{n,disk} &= \sum_{b=1}^{N}\sum_{i=1}^{e} F_{L,i}\cos(\phi_i) + F_{D,i}\sin(\phi_i) \approx \sum_{b=1}^{N}\sum_{i=1}^{e} F_{L,i}\cos(\tan^{-1}(\frac{u_i}{\Omega r_i})) \\ F_{\theta,disk} &= \sum_{b=1}^{N}\sum_{i=1}^{e} F_{L,i}\sin(\phi_i) - F_{D,i}cos(\phi_i) \approx \sum_{b=1}^{N}\sum_{i=1}^{e} F_{L,i}\sin(\tan^{-1}(\frac{u_i}{\Omega r_i})) \end{aligned} \tag{3.6}$$

with N the number of blades. The lift force for each blade element with chord length c_i and length Δr_i can be calculated by:

$$F_{L,i} = \frac{1}{2}\rho V_{rel,i}^2 c_i \Delta r_i C_L(\alpha_i) \tag{3.7}$$

with the relative velocity $V_{rel,i}$ defined as:

$$V_{rel,i} = \sqrt{u_i^2 + (\Omega r_i)^2} \tag{3.8}$$

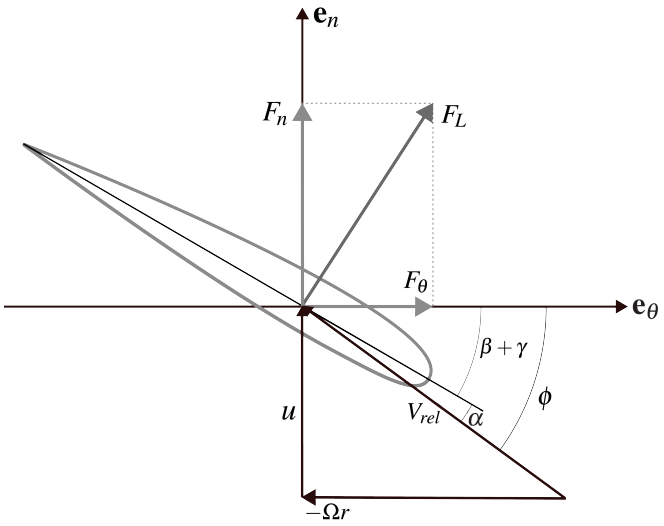

Figure 3.2: Blade element i with corresponding vectors and angles.

Plugging Equations 3.7 and 3.8 into Equations 3.6 and using the trigonometric identities $\cos(\tan^{-1}(x)) = 1/\sqrt{1+x^2}$ and $\sin(\tan^{-1}(x)) = x/\sqrt{1+x^2}$, we find:

$$F_{n,disk} = \frac{\rho\Omega}{2}\sum_{b=1}^{N}\sum_{i=1}^{e} r_i c_i \Delta r_i C_L(\alpha_i)\sqrt{u_i^2+(\Omega r_i)^2} \tag{3.9}$$

$$F_{\theta,disk} = \frac{\rho}{2}\sum_{b=1}^{N}\sum_{i=1}^{e} u_i c_i \Delta r_i C_L(\alpha_i)\sqrt{u_i^2+(\Omega r_i)^2} \tag{3.10}$$

When the Helix is applied, the coefficient of lift for each blade element changes as a result of the changing blade pitch angle. This effect is approximated by a first order Taylor expansion of the coefficient of lift around $\alpha_{i,0} = \phi_i - \gamma_i$. Thereby it is assumed that the angle of attack remains below the onset of stall and changes in induced velocities are ignored.

$$C_L(\alpha_i) = C_L(\alpha_{i,0}) + (\alpha_i - \alpha_{i,0})\frac{dC_L}{d\alpha}\bigg|_{\alpha_{i,0}} = C_L(\alpha_{i,0}) + \beta_b\frac{dC_L}{d\alpha}\bigg|_{\alpha_{i,0}} \tag{3.11}$$

In the remainder of this report, the lift slope will be denoted by $C_{L\alpha}$. Now, for $St = 0$, Equation 3.5 simplifies to $\beta_b(t) = \pm A\sin(\theta_{0,b} + 2\pi f_r t)$. Using that $\theta_b(t) = \theta_{0,b} + 2\pi f_r t$ we can express the blade pitch angle as a function of its azimuthal position:

$$\beta_b(\theta_b) = \pm A\sin(\theta_b) \tag{3.12}$$

Note that the blade pitch angles of all three blades vary sinusoidally and are mutually equal as a function of azimuthal position. This means that the pitch angle only depends on azimuthal position and not on blade number. After plugging this into Equation 3.11 we get an expression for the distribution of C_L in azimuthal direction.

$$C_L(\alpha_i, \theta) = C_L(\alpha_{i,0}) \pm A\sin(\theta) C_{L\alpha}(\alpha_{i,0}) \tag{3.13}$$

Substituting this into Equation 3.9 with $N = 3$ will give the distribution of the perturbed thrust force $F_{n,pert}$ after the Helix is applied:

$$F_{n,pert}(\theta) = F_{n,disk} \pm \frac{3\rho\Omega A\sin(\theta)}{2}\sum_{i=0}^{e} r_i c_i C_{L\alpha}(\alpha_{i,0})\Delta r_i\sqrt{u_i^2+(\Omega r_i)^2} \tag{3.14}$$

In principle, this expression describes the azimuthal distribution of the thrust force that we were looking

for. It is depending on variables that are known throughout the simulation, except for the lift slope and chord length as a function of r. These radial profiles can be user defined functions. In this research we will again use the profiles defined for the IEA 15MW reference turbine (Gaertner et al., 2020). To be generally applicable, turbine variables are made dimensionless by introducing $r' = r/R$ and $c' = c/R$. Next to this, the turbine blade is divided into infinitesimally blade elements allowing for continuous profiles. This converts the sum to an integral:

$$F_{n,pert}(\theta) = F_{n,disk} \pm \frac{3\rho A \sin(\theta)\Omega R^3}{2} \int_0^1 r' c'(r') C_{L\alpha}(r') \sqrt{u(r')^2 + (\Omega R r')^2} dr' \tag{3.15}$$

To approximate the radial variation of the axial velocity u, the thrust force distribution defined by f_c is used. It is assumed that the axial induction, and hence the axial velocity, is linearly related to the thrust force. This means that regions of high thrust force yield a lower axial velocity and vice versa. Therefore, the axial velocity will be distributed as $1 - f_c + K$ in radial direction. Here K is a normalization constant ensuring that integration from $r' = 0$ to $r' = 1$ equals 1. Now, the axial velocity at r' can be approximated as $u(r') \approx u_d(1 - f_c(r') + K)$. Finally, in order to conserve the force applied to the disk, the expression for $F_{n,pert}$ should be normalized. This normalization is straight forward since the total thrust exerted on the disk remains equal to $F_{n,disk}$ after applying the Helix. This follows directly from assuming only first order perturbations in the coefficient of lift. Normalization results in the following expression for the thrust HPK $\mathscr{H}_n$:

$$\mathscr{H}_n(\mathbf{x}) = \frac{F_{n,pert}(\theta(\mathbf{x}))}{F_{n,disk}} = 1 \pm \frac{3\rho A \sin(\theta(\mathbf{x}))\Omega R^3}{2F_{n,disk}} \int_0^1 r' c'(r') C_{L\alpha}(r') \sqrt{u(r')^2 + (\Omega R r')^2} dr' \tag{3.16}$$

A similar derivation of the azimuthal HPK $\mathscr{H}_\theta$ results in:

$$\mathscr{H}_\theta(\mathbf{x}) = 1 \pm \frac{3\rho A \sin(\theta(\mathbf{x}))R^2}{2F_{\theta,disk}} \int_0^1 u(r') c'(r') C_{L\alpha}(r') \sqrt{u(r')^2 + (\Omega R r')^2} dr' \tag{3.17}$$

3.2.2. Time dependence

The HPKs describe the distribution of forces in azimuthal direction for a steady-state situation where $St = 0$. However, when $St \neq 0$ these derived distributions should rotate around with frequency f_e following Equations 3.3 and 3.4. This creates a time dependence of the azimuthal positions θ described by

$$\theta(\mathbf{x}, t) = \theta_0(\mathbf{x}) \pm 2\pi f_e t \tag{3.18}$$

Please note that this function accounts for the Helix excitation period; i.e. the azimuthal positions of the LES grid cells do not physically change. Plugging this into the expressions for the HPKs, we find:

$$\mathscr{H}_n(\mathbf{x}, t) = 1 \pm \frac{3\rho A \sin(\theta_0(\mathbf{x}) \pm 2\pi f_e t)\Omega R^3}{2F_{n,disk}} \int_0^1 r' c'(r') C_{L\alpha}(r') \sqrt{u(r')^2 + (\Omega R r')^2} dr' \tag{3.19}$$

$$\mathscr{H}_\theta(\mathbf{x}, t) = 1 \pm \frac{3\rho A \sin(\theta_0(\mathbf{x}) \pm 2\pi f_e t)R^2}{2F_{\theta,disk}} \int_0^1 u(r') c'(r') C_{L\alpha}(r') \sqrt{u(r')^2 + (\Omega R r')^2} dr' \tag{3.20}$$

In order to discuss the HPKs later on, we note that these HPK expressions can be rewritten to $\mathscr{H}_n(\mathbf{x}, t) = 1 \pm A_n(t)\sin(\theta(\mathbf{x}, t))$ and $\mathscr{H}_\theta(\mathbf{x}, t) = 1 \pm A_\theta(t)\sin(\theta(\mathbf{x}, t))$. Here A_n is called the thrust HPK amplitude and A_θ the azimuthal HPK amplitude. Finally, to create the H-ADM we need to combine the distribution of forces over the disk area from the U-ADM with the azimuthal and temporal distributions from the HPKs:

$$\mathbf{f}^{WT}(\mathbf{x}, t) = \frac{\mathscr{R}^N(\mathbf{x})}{v(\mathbf{x})} \left[\mathscr{H}_n(\mathbf{x}, t) F_{n,disk} \mathbf{e}_\perp + \mathscr{H}_\theta(\mathbf{x}, t) F_{\theta,disk} \mathbf{e}_\theta(\theta_0(\mathbf{x}), \Omega) \right] \tag{3.21}$$

Note that the HPKs already integrate to 1, which means they do not require an additional normalization like the Gaussian projection kernel $\mathscr{R}$. A snapshot in time of the newly obtained thrust force distribution with a HPK amplitude of 0.3 is shown in Figure 3.3. Following Equation 3.21 this distribution rotates around in CCW or CW direction with a frequency equal to f_e.

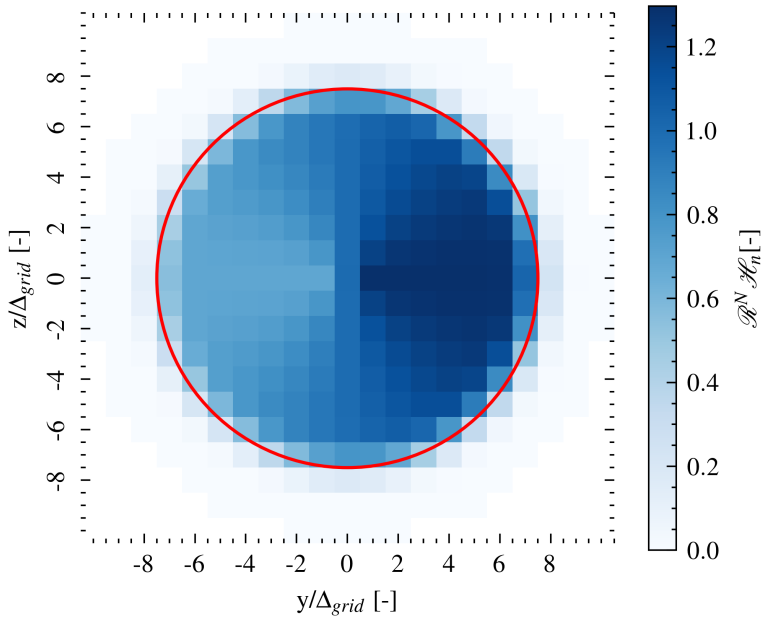

Figure 3.3: Cross sectional view of the force distributions obtained with the H-ADM with a HPK thrust amplitude equal to 0.3. The disk is oriented perpendicular to the streamwise direction and the center is located at x = y = z = 0. The red circle indicates the rotor area.

3.3. Radial force distribution

The obtained force distribution shown in Figure 3.3 seems to capture everything we were looking for. The forces are distributed non-uniformly in azimuthal direction following a sine shape and the amplitude of this sine is derived from BE theory. Therefore, the model should be able to adapt to varying model parameters such as different Helix amplitudes, Strouhal numbers, inflow conditions, etc. This expected behaviour will be validated later in the report. However, one problem with the current definition of the H-ADM remains: around r/R = 0 we observe a steep force gradient. This leads to numerical instabilities in the simulation.

There are different ways to solve this problem. In this research, it is chosen to impose a radial dependence on the force distribution. A common way to model this distribution is by incorporating Prandtl's tip-loss factor for the blade tip and root, as described in Burton et al. (2001). The Prandtl loss factor corrects the uniform force distributions for the loss of lift near the tips of the rotor blade (Prandtl, 1921). This loss of lift force is the result of tip vortices. A similar effect takes places at the root of the turbine blade. An approximation for the Prandtl tip-loss function was introduced by Glauert (1935). Combining both the Glauert tip loss and root loss function, we get the correction function f_c:

$$f_c(r) = \frac{2}{\pi}\cos^{-1}\left(\exp-\left(\frac{N(R_{tip}-r)}{r\sin(\phi)}\right)\right)\frac{2}{\pi}\cos^{-1}\left(\exp-\left(\frac{N(r-R_{root})}{R_{root}\sin(\phi)}\right)\right) \tag{3.22}$$

with N the number of blades, R_{tip} and R_{root} the radii at the blade tip and root and ϕ the local flow angle. It is not trivial to incorporate this in our H-ADM since we would require detailed blade information. To overcome this, we assume that the correction function is independent of Reynolds number and blade geometry. This allows us to pre-define a correction function that can be kept constant throughout the simulation. The distribution that will be used in this research is derived from Moens et al. (2018). In their research they show the correction function for the NREL 5MW turbine at different tip-speed ratios λ. To approximate the correction function at $\lambda = 9$ rpm, i.e. the design tip speed ratio of the IEA 15MW reference turbine, the correction functions from Moens et al. (2018) at $\lambda = 7.55$ and $\lambda = 10.24$ are used to compute a weighted average. The result is shown in Figure 3.4. Similar to Shen et al. (2005) and Pirrung and van der Laan (2018), f_c will be used to determine the distribution of forces in radial direction. Applying this distribution to the LES grid is done using the corrected Gaussian

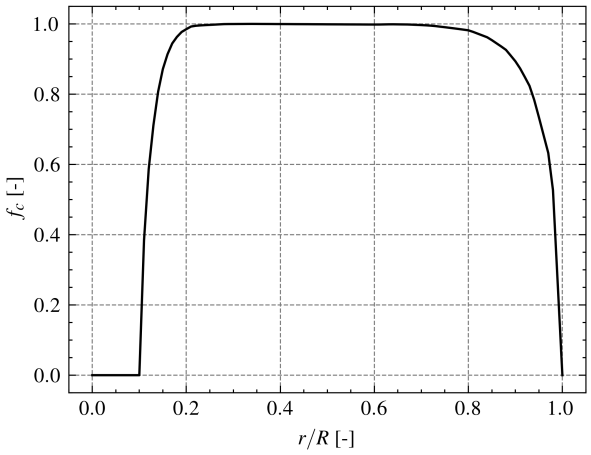

Figure 3.4: The Glauert tip- and root-loss correction function assumed for the IEA 15MW reference turbine.

projection kernel $\mathscr{R}_c$:

$$\mathscr{R}_c(\mathbf{x}) = \iiint f_c(r(\mathbf{x}')/R)S(\mathbf{x}')G(\mathbf{x}-\mathbf{x}')\delta(\mathbf{e}_n\cdot(\mathbf{x}'-\mathbf{x}_0))H(R-\|\mathbf{y}(\mathbf{x}'-\mathbf{x}_0)\|)\,d^3\mathbf{x}' \tag{3.23}$$

with $r(\mathbf{x}') = \|\mathbf{x}'-\mathbf{x}_0-((\mathbf{x}'-\mathbf{x}_0)\cdot\mathbf{e}_n)\mathbf{e}_n\|$ the radial distance between $\mathbf{x}'$ and $\mathbf{x_0}$. Similar to Equation 2.13, the corrected projection kernel should be normalized resulting in $\mathscr{R}_c^N$. The corrected projection kernel is incorporated in the H-ADM by simply swapping it with the old Gaussian projection kernel:

$$\mathbf{f}^{WT}(\mathbf{x},t) = \frac{\mathscr{R}_c^N(\mathbf{x})}{v(\mathbf{x})}\left[\mathscr{H}_n(\mathbf{x},t)F_{n,disk}\mathbf{e}_\perp + \mathscr{H}_\theta(\mathbf{x},t)F_{\theta,disk}\mathbf{e}_\theta(\theta_0(\mathbf{x}),\Omega)\right] \tag{3.24}$$

The new H-ADM without instabilities in the center is depicted in Figure 3.5, again for $D = 15\Delta_{grid}$ and $\alpha = 2$.

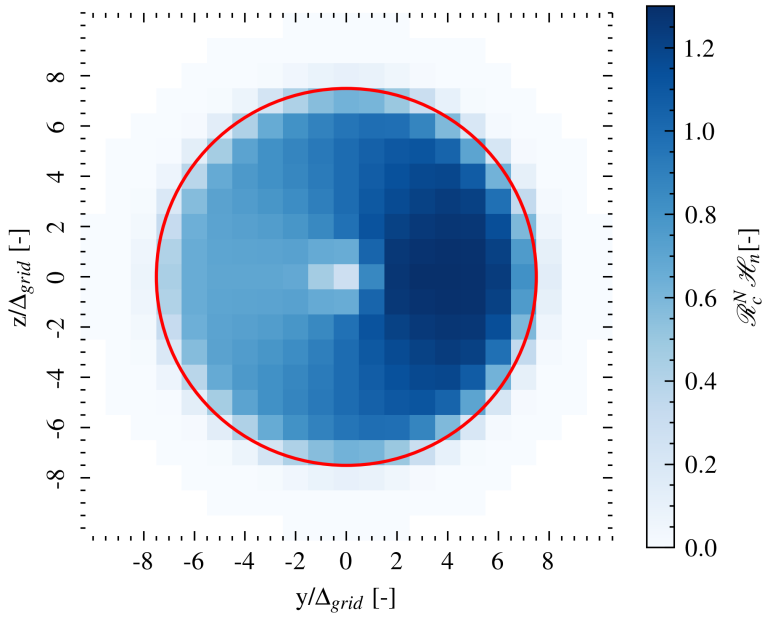

Figure 3.5: Cross sectional view of the force distributions obtained with the H-ADM with a HPK thrust amplitude equal to 0.3. This new version of the H-ADM removes the numerical instabilities at the rotor center. The disk is oriented perpendicular to the streamwise direction and the center is located at x = y = z = 0. The red circle indicates the rotor area.

4

Verification and validation

This chapter will focus on verification and validation of the developed H-ADM. Section 4.1 discusses how the simulations are set up. Then, Section 4.2 researches the H-ADM at a fine resolution and verifies if it is valid for varying simulation variables. The effect of resolution is studied in Section 4.3. Section 4.4 aims to understand the H-ADM performance at different Strouhal number. Finally, Section 4.5 verifies the H-ADM in turbulent conditions.

4.1. Simulation setup

4.1.1. OpenFast

In order to validate the H-ADM, its results will be compared to higher fidelity ALM simulations. The by NREL developed open-source tool OpenFast will be used for this (Jonkman, 2013; OpenFAST, n.d.). OpenFast provides capabilities for simulating the aerodynamics, structural dynamics, control systems and other aspects of wind turbine operation. Those aspects are split in different modules. This work employs the following modules:

- AeroDyn. This module is used to calculate the aerodynamic loads on the turbine blades. The turbine blades are discretized by defining nodes over the span. This research splits the IEA 15MW reference turbine blade into 100 nodes by linear interpolation. For each node two dimensional airfoil look-up tables are available documenting the lift and drag coefficients. BE theory is used to calculate the resulting aerodynamic force on each node.
- ElastoDyn. This module is designed to simulate the structural dynamics of the wind turbine. It computes the response of the turbine structure to the applied aerodynamic loads. This research disables all the degrees of freedom for the turbine blades. This means that a rigid turbine is modelled.
- ServoDyn. ServoDyn is responsible for modeling the turbine's control. This includes the pitch control system, the yaw control system and the generator torque control. The Helix control is applied by using active wake control based on the Coleman transform method.

4.1.2. Coupling to GRASP

The H-ADM has been developed as a plugin to GRASP. This means that the model retrieves the full LES velocity field at each timestep using the ASPIRE interface. It then calculates the velocity tendencies and sends that back to GRASP. To make a fair comparison between the ADM and OpenFast ALM, the two models should be applied in the same GRASP simulation environment. Taschner et al. (2023) created a plugin called AspFast that enables this by coupling OpenFast to GRASP. A schematic of AspFast is shown in Figure 4.1. AspFast retrieves the full LES velocity field from GRASP through ASPIRE, then samples the velocity at the blade nodes and sends that to OpenFast. The OpenFast modules use this information to calculate the aerodynamic forces on each node which is received again by AspFast. AspFast then calculates the projection of these forces onto the LES grid and sends that back to GRASP via ASPIRE.

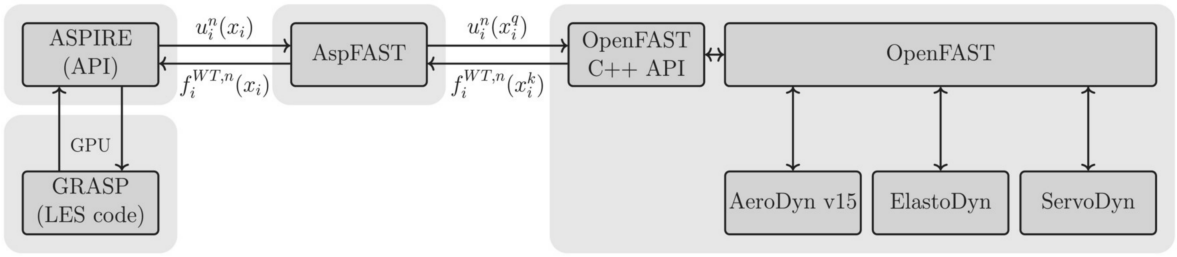

Figure 4.1: Schematic showing how AspFast couples OpenFast to GRASP. Superscripts x^k and x^q denote the kth force and qth velocity actuator point. The superscript $(..)^n$ corresponds to timestep n. Figure from Taschner et al. (2023).

AspFast projects the forces on the LES grid using a Gaussian convolution, similar to the approach of the H-ADM following Equation 3.23. However, there is one subtle difference between G (i.e. the Gaussian kernel used in the H-ADM) and the ALM Gaussian kernel G_{ALM}:

$$G_{ALM}(x) = \frac{1}{\pi^{3/2}\varepsilon_{ALM}^3}\exp\left(-\frac{\|x\|^2}{\varepsilon_{ALM}^2}\right) \tag{4.1}$$

with $\varepsilon_{ALM} = \alpha\Delta_{grid}$. When equating G and G_{ALM} (i.e. both models apply the same smoothing kernel), one finds that ε and ε_{ALM} are offset by a factor of $\sqrt{6}$: $\varepsilon = \sqrt{6}\varepsilon_{ALM}$. Troldborg (2009) found that for the ALM kernel the value of α should meet the criteria $\alpha \geq 2\Delta_{grid}$ to avoid numerical instabilities. For the ADM this criteria is a bit more relaxed: Calaf et al. (2010) found that $\alpha \geq 1.5\Delta_{grid}$ ensures numerical stability.

4.1.3. Domain and turbine settings

To assess the performance of the H-ADM, the turbine and wake behaviour of a single IEA 15MW reference turbine (D = 240 m) will be researched for different simulation conditions. For clarity, each simulation case has been given a name to refer to. This is shown in Table 4.1. Here $\alpha = 2.5$ for the ALM is chosen such that we satisfy the stability condition. Then, in order to apply the same degree of force spreading in the ADM simulations, we use $\varepsilon = \sqrt{6}\varepsilon_{ALM}$ to find that $\alpha = \sqrt{6}\cdot 2.5 = 6.12$.

Unless stated otherwise, the inflow conditions are laminar (i.e. TI = 0.0%) and in streamwise direction. The free stream velocity equals 9 m/s and the turbine is oriented perpendicular to the flow. For these conditions $C_T = 0.78$, $C_P = 0.46$ and $\Omega = 6.41$ rpm. The density ρ equals 1.225 kg/m^3. If the Helix is active, a Strouhal number of 0.25 and amplitude A of 2° is used. For the NH simulations A is simply set to 0° in the H-ADM. The L60 simulations use a timestep $\Delta t = 0.02$ s. The ADM simulations use a timestep that ensures the Courant-Friedrich-Levy number (CFL) to be below 0.9. For a velocity of 9 m/s and a gridsize of D/15, with D = 240 m, this equals an ADM timestep of $\Delta t = 1.6$ s. This illustrates that, for this specific ADM gridsize and maximum domain velocity, the simulation requires factor 80 fewer steps than the ALM simulation. For both simulations, the total simulation time is 1200 s. Finally, the Smagorinsky SGS model is used with Smagorinsky constant $C_s = 0.16$ (Smagorinsky, 1963). The domain settings for different gridsizes Δ_{grid} are listed in Table 4.2. Here the streamwise length L_x of the domain is shorter for $\Delta_{grid} = D/60$ due to computational constraints. The turbine is placed in the center of the yz-plane to remove ground effects.

For the H-ADM, radial profiles of the chord length and lift slope are model inputs. In this research, these are derived by fitting polynomials to the discrete profiles of the IEA 15MW reference turbine (Gaertner et al., 2020). The resulting continuous profiles are shown in Figure 4.2 and further discussed in Appendix A.

Table 4.1: Simulation parameters for the different cases

Case name	Model type	Helix	Δ_{grid}	α
L60NH	ALM	No	D/60	2.5
L60CCW	ALM	CCW	D/60	2.5
L60CW	ALM	CW	D/60	2.5
D60NH	ADM	No	D/60	6.12
D60CCW	ADM	CCW	D/60	6.12
D60CW	ADM	CW	D/60	6.12
D30CCW	ADM	CCW	D/30	6.12
D30CW	ADM	CW	D/30	6.12
D20CCW	ADM	CCW	D/20	6.12
D20CW	ADM	CW	D/20	6.12
D15NH	ADM	No	D/15	6.12
D15CCW	ADM	CCW	D/15	6.12
D15CW	ADM	CW	D/15	6.12

Table 4.2: Domain setup for different gridsizes

Δ_{grid}	L_x	L_y	L_z	x_{hub}	y_{hub}	z_{hub}	L_n	η
D/60	21.3D	6D	6D	5.8D	3D	3D	D	0.95
D/30	38.4D	6D	6D	5.8D	3D	3D	2D	0.95
D/15	38.4D	6D	6D	5.8D	3D	3D	2D	0.95
D/10	38.4D	6D	6D	5.8D	3D	3D	2D	0.95

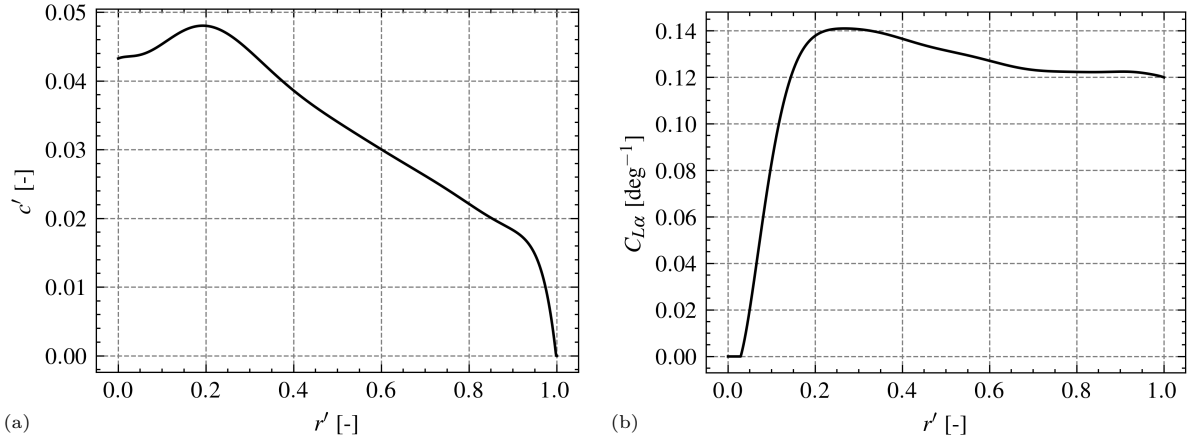

Figure 4.2: The radial profiles for the dimensionless chord length c' (a) and the lift slope $C_{L\alpha}$ (b) used in the H-ADM.

4.2. Model performance at fine resolution

4.2.1. Amplitude sensitivity

To assess the wake recovery simulated by both the ALM and H-ADM, the time averaged power recovery will be calculated at each $\Delta x = D/2$ as $P_r^s(x) = \left\langle u_w^3(x,t) \right\rangle / u_\infty^3$. Here u_w is the average wake velocity calculated by sampling in a cylinder aligned with the rotor axis, i.e. a static reference frame right behind the turbine. The time averaging period is five Helix periods $5/f_e$ with 1 second interval data.

As expected, the simulation results are sensitive for different HPK amplitude values A_n and A_θ. This effect can be observed in Figure 4.3, where two sets of simulations using the D15CCW setup are executed. The sensitivities of A_n and A_θ are isolated by varying one of the two amplitudes, while keeping the value of the other amplitude fixed at 0.14. At $x/D = 5$ the power recovery decreases by 22.6% when moving from a thrust amplitude of 0.18 to 0.12. This indicates that the thrust amplitude sensitivity is something to be aware of since it significantly influences the simulated wake recovery. The effect of varying the azimuthal amplitude is less pronounced. An interesting observation is the fact that a higher azimuthal amplitude, i.e. a more skewed distribution of the azimuthal force, leads to a slower wake recovery, opposing the trend observed for the thrust amplitude.

Since results are very sensitive for the HPK amplitude values, the amplitudes are calibrated using the results of ALM simulations. By investigating individual blade output data it is found that $A_n = 0.139$ for the L60-CCW case. However, the D60CCW case finds $A_n = 0.194$. This means that the H-ADM overestimates the thrust HPK amplitude by almost 29% for this simulation case. Upon further analysis of the ALM data, it turns out this overestimation is mainly caused by:

1. Both the thrust and azimuthal forces calculated by the ADM are lower compared to the ALM forces. This causes an underestimation of the denominator in the HPK calculation.
2. For each radial position, the lift slope profile from Figure 4.2 overestimates its values compared to ALM results. It is hypothesized that this is the effect of unsteady aerodynamics that are being modelled by OpenFast and are not incorporated in the ADM.

For this reason, both HPK amplitudes are calibrated by rescaling them with a correction factor A_c of $A_c = 1\text{-}0.29 = 0.71$. The rescaling factor accounts for the underestimation of forces by the ADM and/or overestimation of forces by the ALM and the unsteady aerodynamics that are not resolved. Later, it will be researched if this rescaling factor remains constant for different simulation parameters, such as a different wind speed, Helix amplitude and Strouhal number.

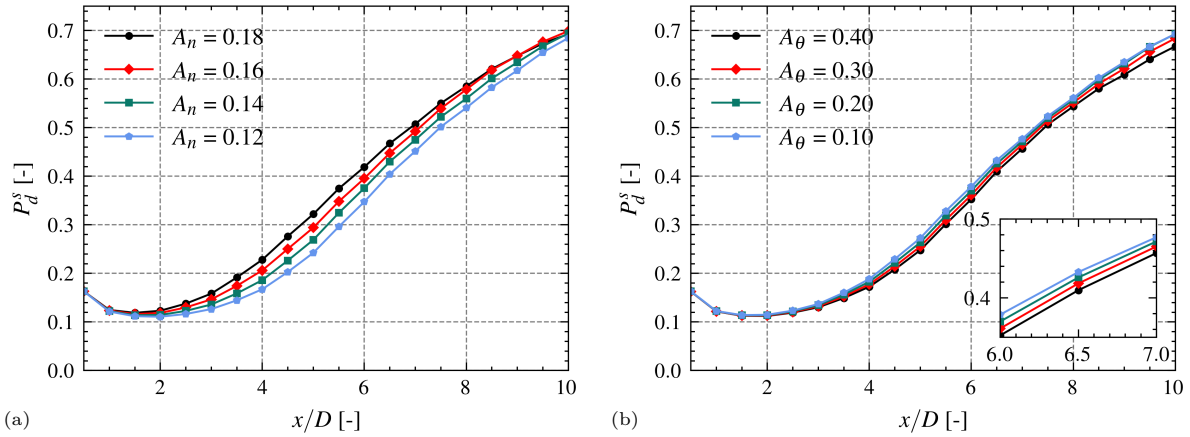

Figure 4.3: The wake recovery process for different values of the thrust (a) and azimuthal (b) HPK amplitudes.

4.2.2. Wake recovery

As a first step in validating the model, we intend to gain insight in the model behaviour at a fine resolution equal to the ALM resolution. This eliminates a gridsize dependence. Figure 4.4 shows the results for the wake recovery predicted by the L60 and D60 cases. Here the recovery bias ΔP_r^s expresses the power recovery difference between the ADM and ALM as a fraction of the ALM power recovery: $\Delta P_r^s = (P_{r,ADM}^s - P_{r,ALM}^s)/P_{r,ALM}^s$. It immediately stands out that data for the L60NH case is only available until $x/D = 7$. This is the result of unreliable data further away from the turbine. For the L60NH case the position of laminar-turbulent transition changes as soon as the wake hits the nudging zone. Taschner et al. (2023) solved this by increasing the domain length to avoid interactions between the wake and the nudging zone. Due to computational limitations this is not possible in this research, meaning we are limited to L60NH data until $x/D = 7$. Looking at the results, it is clear that the power recovery estimated by the D60NH case is larger than the L60NH case. This again is mainly caused by the ALM overestimating and/or ADM underestimating the turbine forces. For the Helix results we note that the

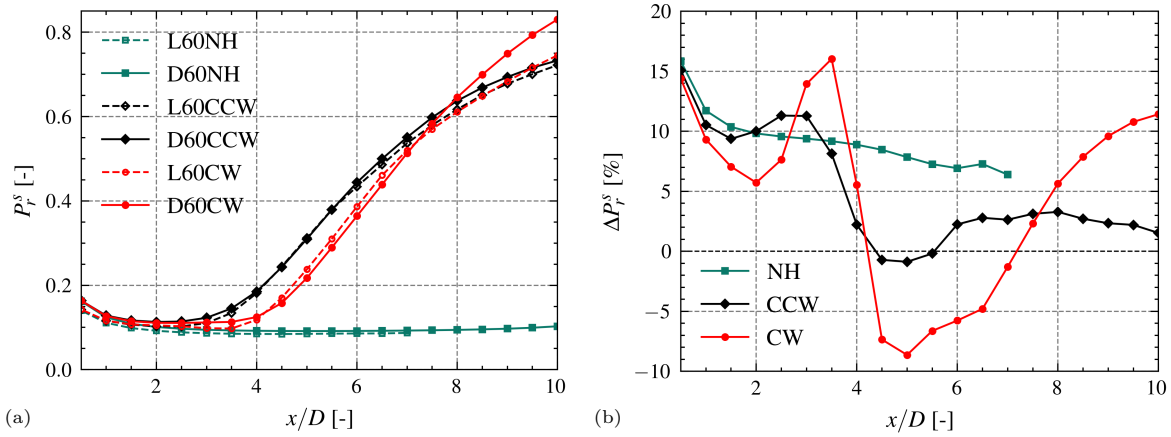

Figure 4.4: The static frame power recovery (a) and the corresponding bias (b) for the L60 and D60 cases.

wake recovery starts at a similar distance behind the turbine for the H-ADM and ALM. This does not immediately match expectations since the H-ADM does not resolve tip-vortices. The tip-vortices create 3D flow structures around the blade tip and are expected to contain the wake, thereby postponing its recovery. It can be argued that the ALM simulations might not resolve detailed tip vortex structures since they are still simulated at a relatively coarse resolution. From x > 3D, the absolute values of the CW and CCW recovery bias start to decrease, even staying below 5% for the CCW case. However, towards the end of the considered domain the D60CW results starts diverging away from L60CW. This eventually leads to a bias slightly larger than 10% around $x/D = 10$. Furthermore, both models predict that the CW Helix eventually outperforms the CCW Helix in terms of wake recovery. For the H-ADM the crossing occurs around 7.8D and for the ALM around 8.7D. The mechanism causing this crossing is not fully understood yet and will be researched later in this report in Chapter 5.

The instantaneous streamwise velocity field at hub height is shown for the L60 and D60 Helix cases in Figure 4.5. It should be noted that the considered simulations have a laminar inflow. This means that the recovery process is initiated and affected by only the turbine model. When simulating turbulent flow, the recovery process is enhanced by turbulent ambient air mixing with the wake. In that case a process that is independent of turbine modelling contributes to the recovery process. Therefore, it is expected that turbulence will cause the difference between the ALM and H-ADM to decrease.

4.2.3. Wake steering and mixing

To further understand the H-ADM and the observed differences for the CW case, we will dive deeper into the mechanisms causing the accelerated Helix wake recovery. Korb et al. (2023) found that the increased wake velocity is caused by both a larger wake deflection and a higher entrainment of kinetic energy into the wake from surrounding flow. The displacement of the wake can be quantified by computing the wake center. This will be done using a velocity-deficit-weighted average method (Quon et al., 2020). The wake center coordinates $y_c(x)$ and $z_c(x)$ are calculated as (Howland et al., 2016):

$$y_c(x) = \frac{\iint y\Delta U(x,y,z)\,dydz}{\iint \Delta U(x,y,z)\,dydz} \quad \text{and} \quad z_c(x) = \frac{\iint z\Delta U(x,y,z)\,dydz}{\iint \Delta U(x,y,z)\,dydz} \tag{4.2}$$

with $\Delta U(x,y,z) = u_\infty - u(x,y,z)$ and a velocity threshold $u(x,y,z) < 0.9u_\infty$. The wake displacement d equals the time averaged radial distance between the rotor center, with coordinates y_{hub} and z_{hub}, and the calculated wake center: $d(x) = \left\langle \sqrt{(y_{hub} - y_c(x))^2 + (z_{hub} - z_c(x))^2} \right\rangle$. Again, the time averaging period equals five Helix periods. Similar to Korb et al. (2023), we can define a new reference frame by translating the rotor area from the static frame towards the displaced wake center. This creates a rotating reference frame that will follow the wake center. A visualization of the wake displacement and the corresponding rotating reference frame is shown in Figure 4.6.

The results for d are plotted in Figure 4.7. The NH wakes do not meander since we are using laminar inflow conditions. This means that $d/D = 0$ which is why the NH results have been left out. It can be seen that the CCW displacement is accurately predicted, with an absolute bias below 5% for most

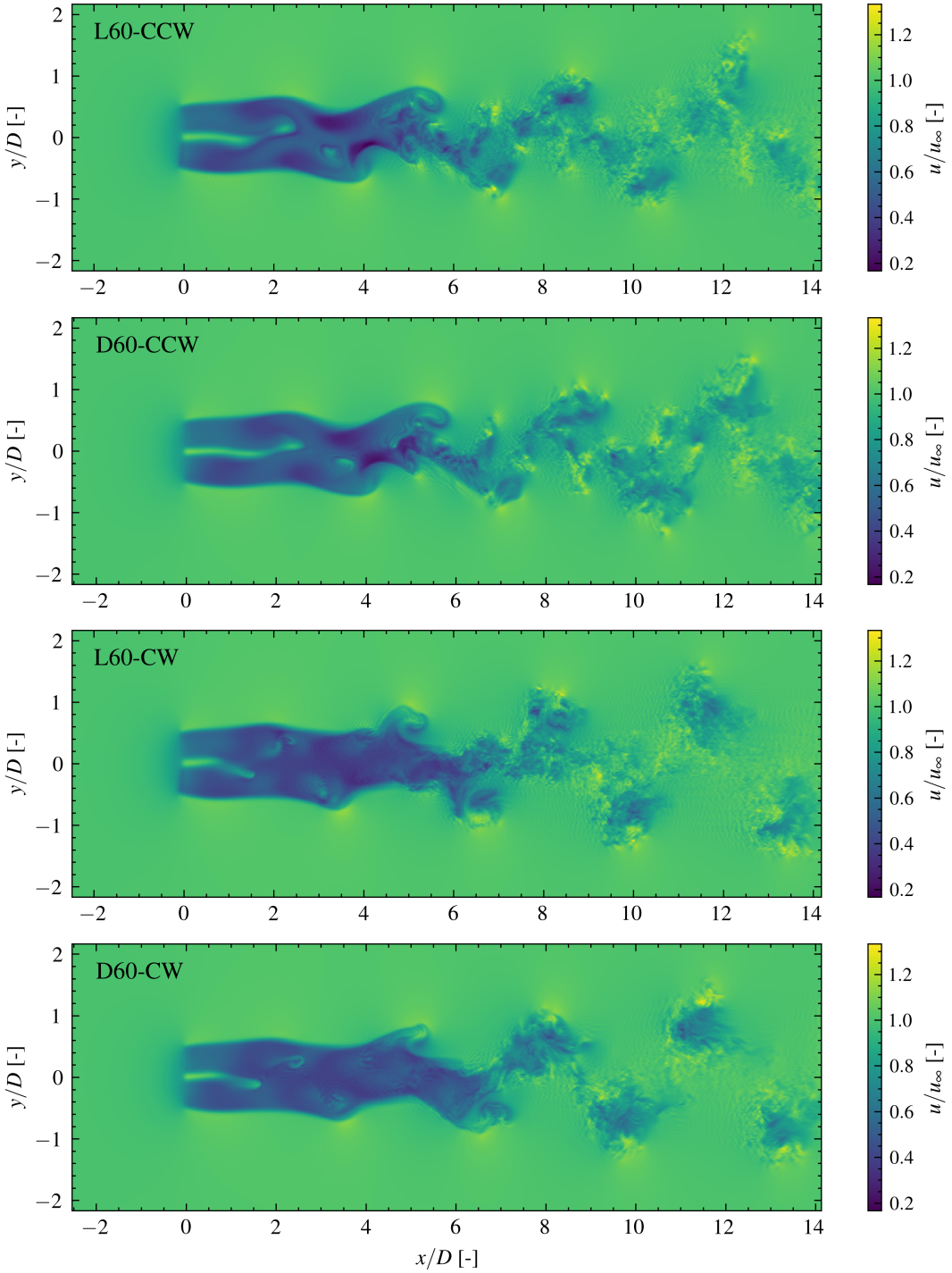

Figure 4.5: Instantaneous streamwise velocity fields for the different L60 and D60 Helix cases.

of the considered domain. Around 9D the results start to diverge. Unfortunately, data availability is limited to $x/D = 10$, meaning we cannot assess if the power recovery continues diverging. For The CW case we observe similar matching behaviour until 7D. From 7D onwards the displacement diverges away from the ALM solution, eventually reaching a bias of almost +15% at 10D. This diverging behaviour matches with what we observed in Figure 4.4 for the CW power recovery. Therefore, it is hypothesized that the observed CW power recovery difference from 7D onwards is caused by an overestimation of the wake displacement. However, this analysis is not exhaustive. For example, the displaced wake could experience a different degree of mixing between both models. This effect also contributes to the power

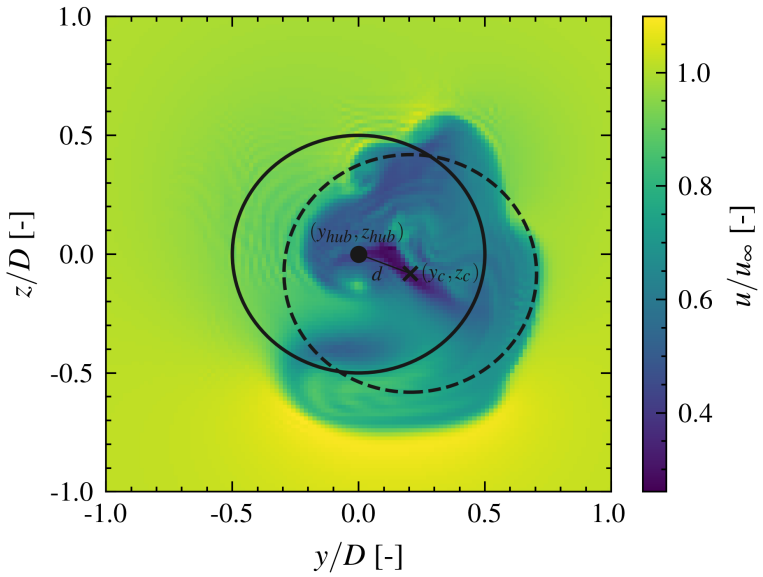

Figure 4.6: Illustration of wake displacement and the corresponding center distance. Instantaneous slice at $x/D = 5$ for the D60CCW case. The black dot and cross represent the static and displaced wake centers, respectively. The corresponding rotor areas are indicated by the solid and dashed circles. The thin black line represents the wake displacement d.

recovery in the static frame since both reference frames overlap ($d/D < 1$).

Therefore, to test this hypothesis further, we examine the power recovery in the rotating frame P_r^r. Those results are shown in Figure 4.8. Similar to the power recovery in the static reference frame, the CCW results are accurate from 4D onwards with an absolute bias of less than 5%. Interestingly, the CW result shows an underestimation of the power recovery from 4D onwards. As a result, the power recovery in the static frame is actually reduced since both reference frames overlap. For this reason, it can be concluded that the diverging behaviour of the CW case static frame power recovery in Figure 4.4 is caused by the overestimation of the wake displacement from 7D onwards. Additionally, the diverging behaviour of this CW case is decelerated by the underestimation of the displaced wake recovery.

It is remarkable that the H-ADM seems to be very accurate for the CCW Helix (i.e. $|\Delta P_r^s| < 5\%$ from $x/D = 4$ onwards) but has some trouble with the CW Helix, especially in the far wake. The CCW agreement proves that the idea of the H-ADM with rotating the HPK distributions works well in CCW direction. Based on the Helix theory one would expect this framework to hold in CW direction as well. To explain the diverging behaviour of the CW Helix, it is hypothesized that this is the result of instabilities maintained in laminar inflow (Coquelet et al., 2024). The advantage of laminar inflow is that

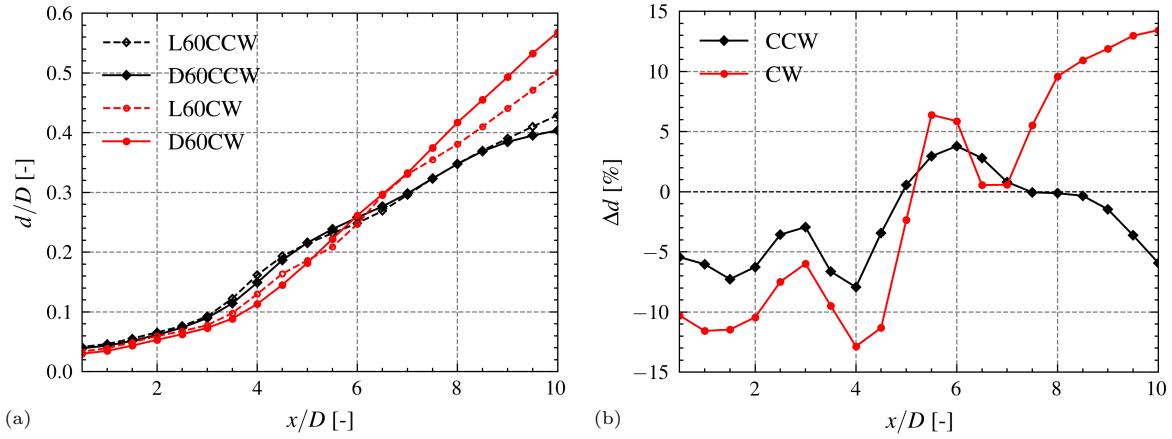

Figure 4.7: The wake displacement (a) and the corresponding bias (b) of the L60 and D60 cases.

it allows for a direct comparison between the ADM and ALM, since there is no additional wake mixing from turbulence. However, at the same time this also has a downside. Due to the absence of ambient turbulence, the wake recovery depends only on the instabilities developing in the wake vortex system. The different vortex structures in the H-ADM CW wake could make it more susceptible for maintained instabilities than the H-ADM CCW or ALM wakes. To verify this and run turbulent simulations with GRASP, the simulation domain needs to develop turbulence which requires time. These simulations will get too expensive at the fine resolution of D60. Therefore, this laminar flow hypothesis will be researched in section 4.5 on a coarser grid.

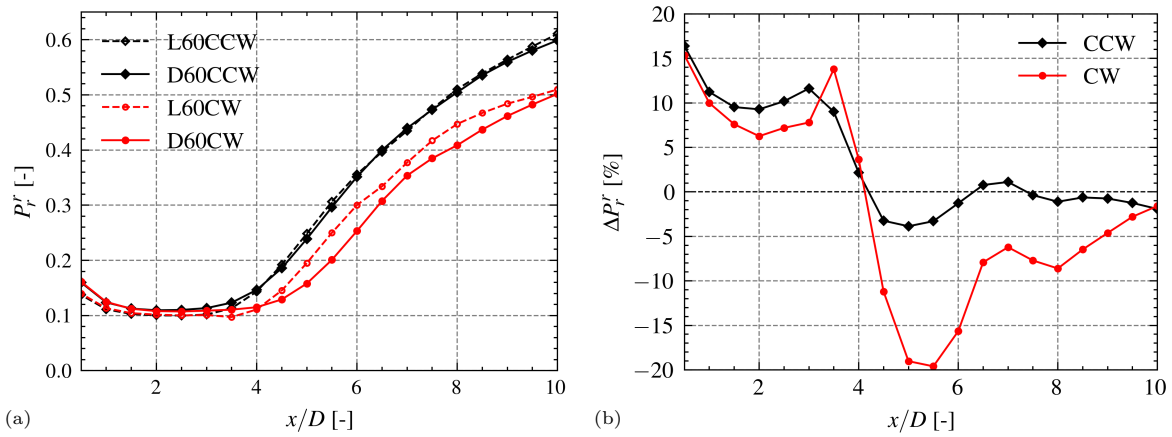

Figure 4.8: The rotating reference frame power recovery (a) and the corresponding bias (b) of the L60 and D60 cases.

4.2.4. Different model conditions

So far, we can conclude that the H-ADM is able to accurately predict the wake recovery of the CCW Helix. It is expected this is the case for the CW Helix as well, but the hypothesis regarding laminar instabilities causing the divergence is not yet verified. By 'accurate' it is meant that the H-ADM simulates the power recovery of the Helix wakes with a bias equivalent to or smaller than the bias of the NH simulation. Here the bias is defined with respect to the ALM, where it should be noted that the ALM also is not perfectly modelling reality. However, it is a higher fidelity model resolving more of the blade structures than the H-ADM, which is why the ALM is set as a benchmark in determining the H-ADM accuracy.

The accurate results of the H-ADM we have seen, are produced after calibrating the model with a rescaling factor A_c. Also, the model has only been tested for one set of model conditions ($u_\infty = 9m/s, St = 0.25, A = 2°$). The goal of this research is to develop an accurate H-ADM that can be applied to wind farm scale simulations. When simulating real weather conditions or using the model to optimize Helix settings, the model conditions are constantly changing. For this reason it is of interest to asses the performance of the H-ADM for varying model conditions.

Ideally, the model keeps simulating the Helix wake recovery accurately, in which case the correction factor A_c can be treated as a turbine constant. However, if this is not the case a look-up table for A_c would be required to apply the model in varying conditions. We have seen before that A_c accounts for unsteady aerodynamics and the difference in forces between the ADM and ALM. The H-ADM is not able to simulate the unsteady aerodynamics included in the ALM, which are expected to vary for changing model conditions. For example, increasing St will increase the blade pitch frequency enhancing the effect of hysteresis. However, the model conditions also influence the rotor forces in both models.

To find out how these effects balance, new H-ADM simulations with different conditions are executed and compared to ALM. The D60CCW and L60CCW cases are used with each time one model condition changing. Table 4.3 shows which variable changes and the corresponding suffix. All variables that are not mentioned remain similar to the setup described in Section 4.1.3. The results are shown in Figure 4.9. It is clear that for all new cases the H-ADM continues simulating accurate results of the wake recovery without changing A_c. The absolute bias remains below 8% from $x/D = 4$ onwards. Based on these results we assume, throughout the rest of this research, that the correction factor A_c is valid across the whole range of model conditions. It would be interesting future research to find the limits of this.

This can for example be done by pushing model conditions to more extreme values, e.g. even higher or lower values for the free-stream velocity, Helix amplitude and Strouhal number.

Table 4.3: The influenced model variables with the corresponding case suffix.

Case name	u_∞	Ω [rpm]	A [°]	St [-]
case-u	7.0	5.0	2	0.25
case-A	9.0	6.4	1	0.25
case-St	9.0	6.4	2	0.375

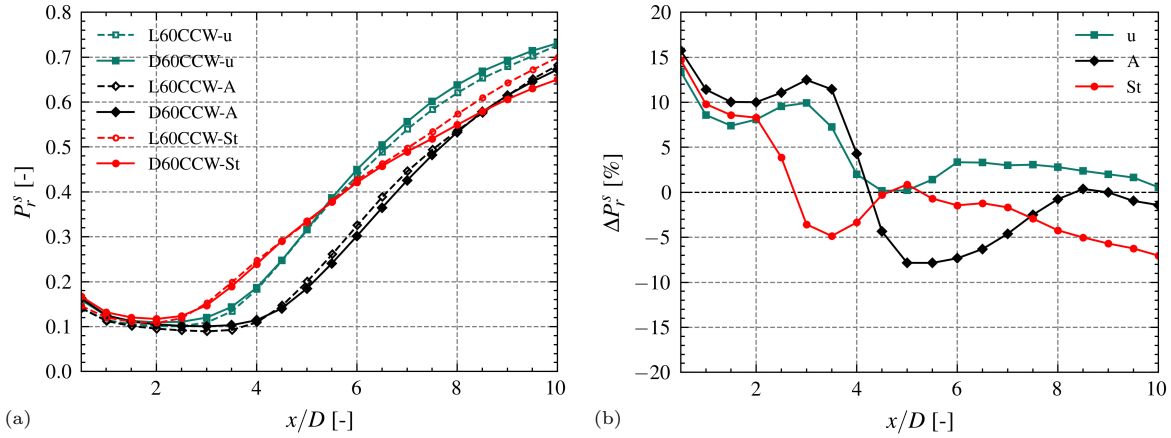

Figure 4.9: The static reference frame power recovery (a) and the corresponding bias (b) for the different model conditions cases.

4.3. Gridsize dependence

The last section made us understand the performance of the H-ADM at a resolution equal to the ALM. Even though the H-ADM is already computationally faster at that fine resolution since the timestep is not constrained by the tip-speed ratio, we are interested in getting to know the model behaviour at a larger grid-size. This section researches how resolutions as low as $\Delta_{grid} = D/15$, a resolution suited for farm size simulations, influence the H-ADM performance.

4.3.1. The effect of force spreading

For different resolution cases, as listed in Tables 4.1 and 4.2, the static frame power recovery is shown in Figure 4.10. The first thing that stands out is that a coarser grid results in a higher power close to the turbine. This is the consequence of the constant value for α used at different resolutions. As a result, the value for ϵ increases with grid-size. This means that the force is less concentrated in the rotor area, resulting in a lower velocity deficit right behind the turbine. Moving further away from the turbine towards the recovery region, it is clear that the slope of the power recovery curve is smaller for a larger grid-size. This is also as expected, since for a larger grid-size a smaller fraction of the flow is resolved. Consequently, there is fewer mixing and wake displacement, as was also observed by for example Réthoré et al. (2014).

Judging by these results, it looks like the Helix cannot be accurately simulated at a coarse resolution. However, since the value for ϵ is not fixed, the force gets spread out over a larger surface when the grid-size increases. As a result, the force gradient ($= dF/dr$) at the edge of the rotor area decreases for a larger grid-size. The force gradient has a large influence on the degree of wake mixing and displacement, the two phenomena that drive the Helix wake recovery. To investigate this effect further, the simulations at different resolutions were repeated with a constant ϵ, ensuring a consistent force gradient. This means

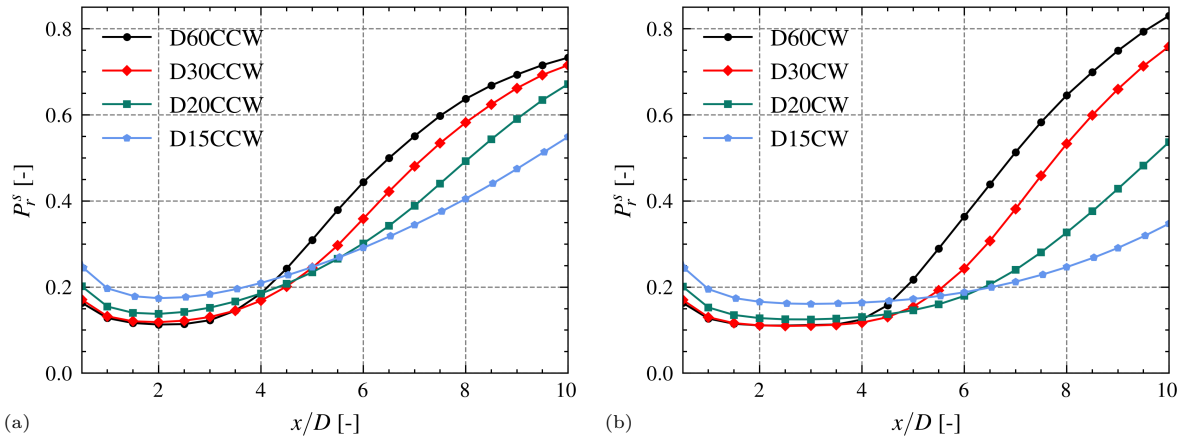

Figure 4.10: The H-ADM gridsize sensitivity of the static reference frame wake recovery for the CCW (a) and CW (b) configurations.

α is grid-size dependent since $\varepsilon = \alpha\Delta_{grid}$. The new values for α corresponding to each grid-size are shown in Table 4.4. The static frame power recovery for these new simulations are shown in Figure 4.11. This shows that the effect of power recovery is still underestimated when the grid-size is increased.

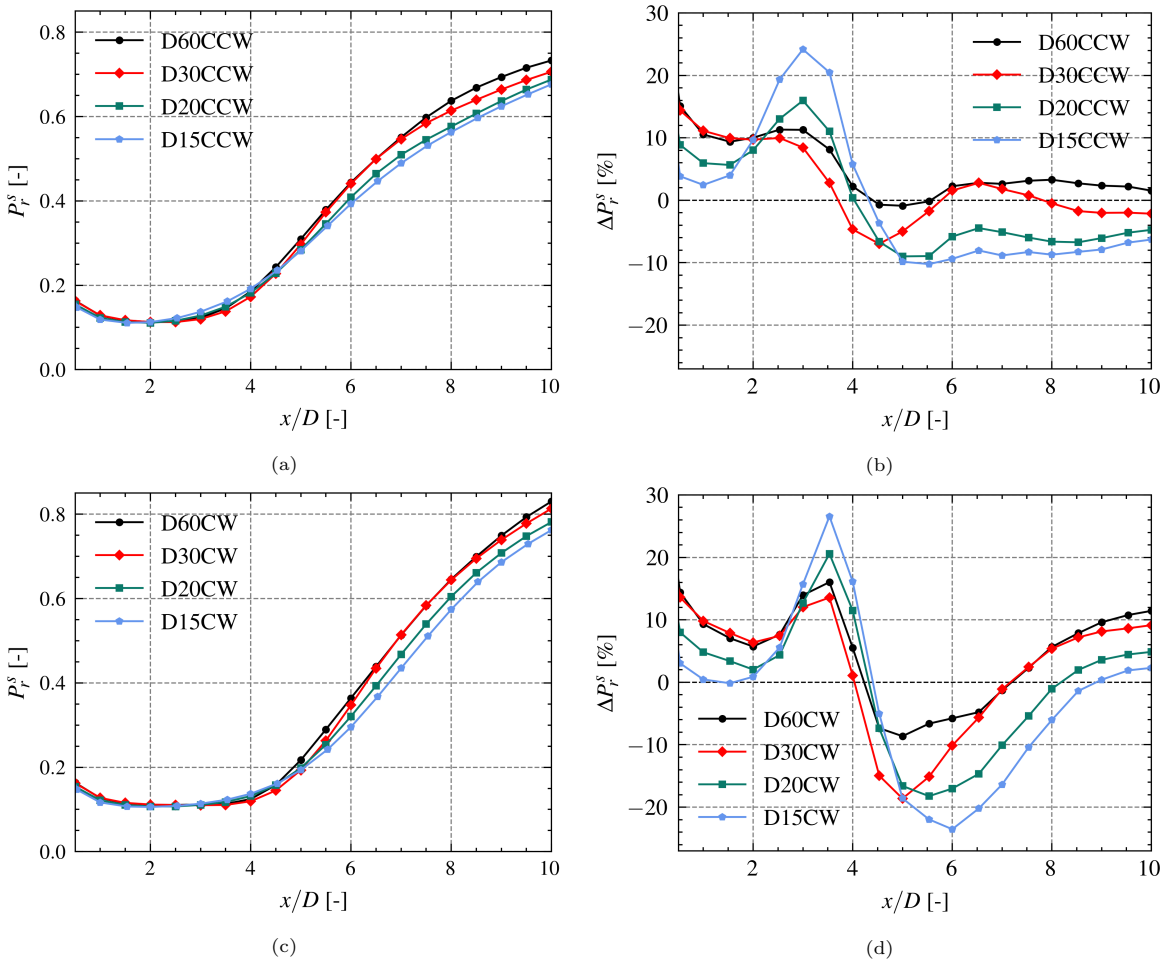

Figure 4.11: The static frame power recovery for different grid-sizes with a constant ε. (a) contains CCW Helix results, with the bias expressed with respect to L60CCW in (b). (c) and (d) show the CW Helix results and the gain defined with respect to L60CW.

Table 4.4: The values of α corresponding to each grid-size for the constant ε simulations.

Δ_{grid}	D/60	D/30	D/20	D/15
α	6.12	3.06	2.04	1.53

However, it is clear that the constant force gradient improved results for all grid-sizes. For the D15CCW case the recovery bias is slowly decreasing from -10% to almost -5% for $x/D > 5$. The D15-CW case shows a little different bias behaviour, where around $x/D = 6$ the absolute bias is at a maximum. Then results quickly improve, with a bias of +2% at $x/D = 10$. For all grid-sizes, the recovery bias seems to be constant from a certain streamwise location x onwards. For the CCW cases this is around $x/D = 5$, and for the CW cases this is around $x/D = 9$. Unfortunately there is no data beyond $x/D = 10$ to verify this. However, this would be an indication that the H-ADM has trouble modelling the initial phase of the Helix wake recovery, but that after that initial phase the H-ADM starts matching the recovery rate predicted by the ALM. This hypothesis is further supported by an observation in the near-wake. It appears that a coarser grid-size triggers an earlier start of the power recovery. However, the finer resolutions quickly catch up due to the larger recovery slopes we observed earlier. These dynamics create the bias overshooting behaviour observed for the coarser grid-sizes around 3D and 5D for the CCW configuration and around 3.5D and 5.5D for the CW configuration.

Apart from improving the coarse resolution results, it is important to note that the fixed force gradient imposes a limitation on the maximum grid-size possible. Since a constant ε is required, α should decrease for an increasing grid-size. Following the recommendation of Calaf et al. (2010), α should be larger than 1.5 to avoid numerical instabilities. That means that for the value of ε chosen in this research, we cannot go much coarser than D/15 since that will violate the stability condition.

4.3.2. Computation time

It is clear that increasing the grid size lowers the accuracy of the H-ADM. However, a benefit of a coarser grid is the reduction of computational time. This section briefly discusses the trade-off between a higher accuracy and a lower computation time. In order to asses the H-ADM accuracy for different grid-sizes, the mean absolute power recovery bias $\langle|\Delta P_r^s|\rangle$ for both Helix configurations over a certain domain will be calculated. This means that the absolute value of ΔP_r^s will be averaged over specified streamwise positions. Then the total mean bias $\langle|\Delta P_r^s|\rangle_{tot}$ will be calculated by averaging the results of the two Helix configurations: $\langle|\Delta P_r^s|\rangle_{tot} = (\langle|\Delta P_r^s|\rangle_{CCW} + \langle|\Delta P_r^s|\rangle_{CW})/2$. Since for most wind farms the turbine spacing is between 5D and 8D, the mean bias will be calculated over the domain $5D \leqslant x \leqslant 8D$. Figure 4.12 shows the results of the total mean bias and computation time as a function of grid-size. Computation time is expressed in GPUm, i.e. the simulation time in minutes on a Nvidia A100 GPU, and shown

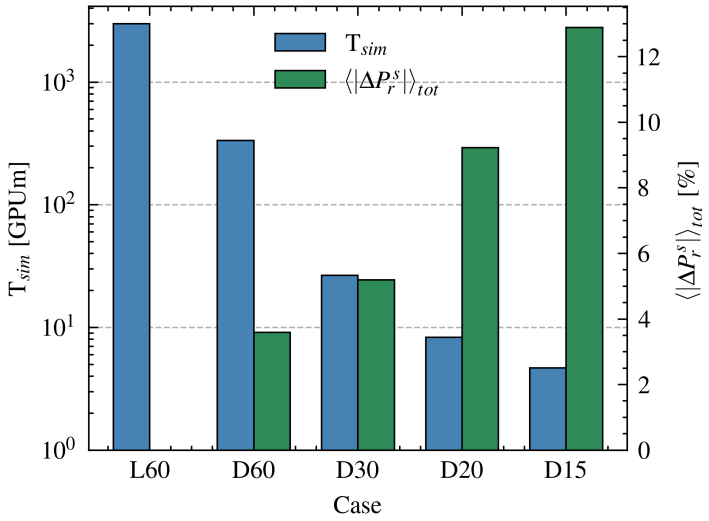

Figure 4.12: The total mean bias and simulation time for the different considered grid-sizes.

on a logarithmic scale. The difference between L60 and D60 immediately stands out. Without even changing the grid-size the H-ADM is already 9x faster. This simulation time reduction is associated with a total mean bias of 3.6%. Moving towards the coarsest resolution considered, D15, we see a gain in computational power of factor 643 compared to L60. Here it should be noted that the simulation domain for L60 is smaller following Table 4.2. This computational gain comes at the expense of the total mean bias reaching almost 13%. It is important to note this can be considered an upper limit of the error. The first reason for this is that differences between the H-ADM and ALM are expected to decrease in turbulent conditions. Secondly, the H-ADM model parameters can be tweaked in order to increase the accuracy in power recovery. An example of a parameter that can be tweaked is the amplitude correction factor A_c. This optimization will be executed in the next section.

4.3.3. Parameter sweep

Last section showed the large computational gains that can be achieved with the H-ADM. Currently, this computational gain comes at the cost of an increased error in the simulated power recovery. This section aims at minimizing this error by executing a parameter sweep. The model variable that will be optimized is the amplitude correction factor A_c. We have already seen that the solution is very sensitive for the value of A_c in Figure 4.3. This property will be used to decrease the error of the D15 simulation.

To assess the performance of each amplitude correction factor A_c, the mean absolute power recovery bias $\langle|\Delta P_r^s|\rangle$ on the domain $5D \leqslant x \leqslant 8D$ will be used as performance metric. First, the mean absolute bias will be calculated for A_c values ranging between 0.6 and 1.2, with intervals of 0.1. Based on these results, a domain of width 0.2 containing the minimal absolute bias is selected. Then a new sweep is executed, where A_c varies over the selected domain with intervals of 0.01. The results for both Helix configurations are shown in Figure 4.13. The optimum values, i.e. the values of A_c minimizing the performance metrics, are found at $A_c = 0.91$ and $A_c = 1.00$ for the CCW and CW case respectively. It is as expected that the optimal correction factor for the CW case deviates most from $A_c = 0.71$, the value used before. This follows from the larger absolute bias between 5D and 8D for the D15CW case in Figure 4.11, indicating it requires a larger correction.

Since we are interested in simulating both the CCW and CW configuration on a farm-size scale, the total mean bias $\langle|\Delta P_r^s|\rangle_{tot}$ will be calculated and used to find a general optimum. This means that we will deviate from the individual optima found before. The results are shown in Figure 4.14. It is clear that the total mean bias between 5D and 8D is minimized for $A_c = 0.95$ with a value of 3.1%. The corresponding power recoveries for the D15CCW and D15CW cases with $A_C = 0.95$ are shown in

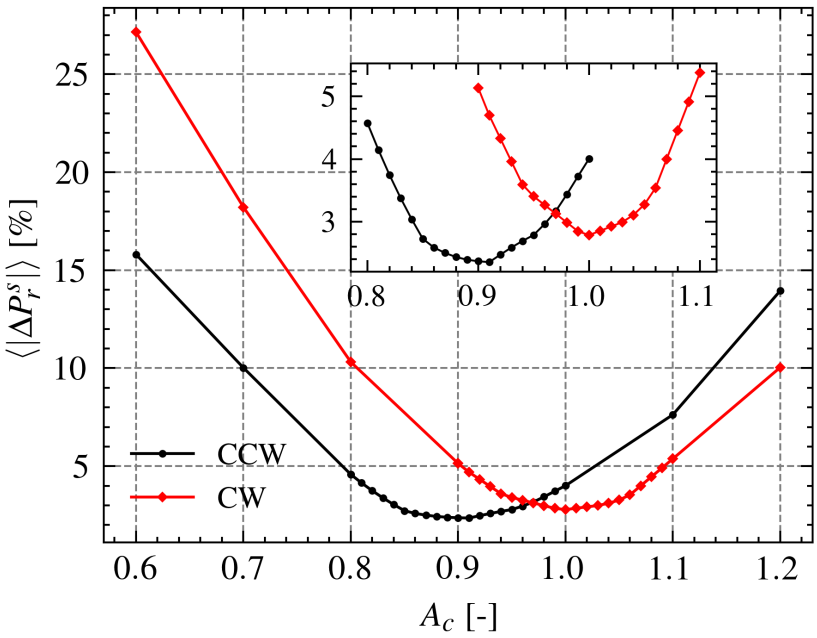

Figure 4.13: Results of the parameter sweep for the D15CCW and D15CW cases.

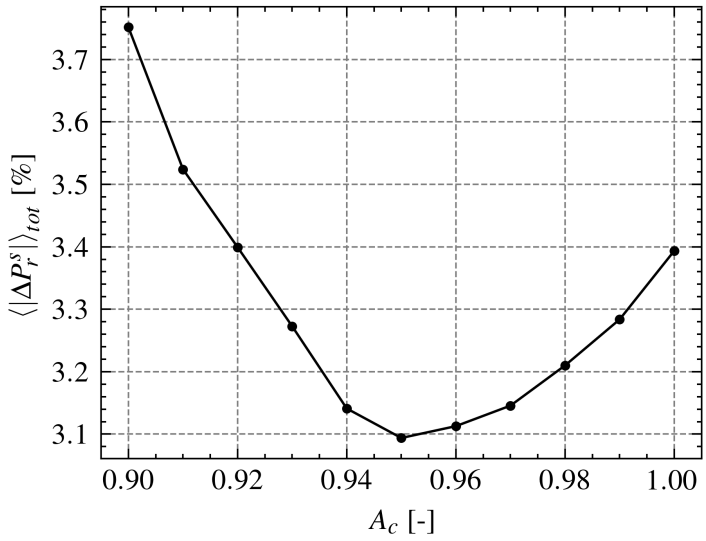

Figure 4.14: Results for the total mean recovery bias for different amplitude correction factors.

Figure 4.15. After the parameter sweep the absolute bias for the D15 cases remains below 7% for the considered domain, with an average of 3.1%. These results are for laminar inflow conditions, and again, it is expected that this bias decreases in turbulent conditions. The most important outcome of this parameter sweep is the fact that the H-ADM can now simulate the Helix wake recovery over 640 times as fast as the ALM with only an average error of 3.1% for the domain $5D \leqslant x \leqslant 8D$ in laminar conditions.

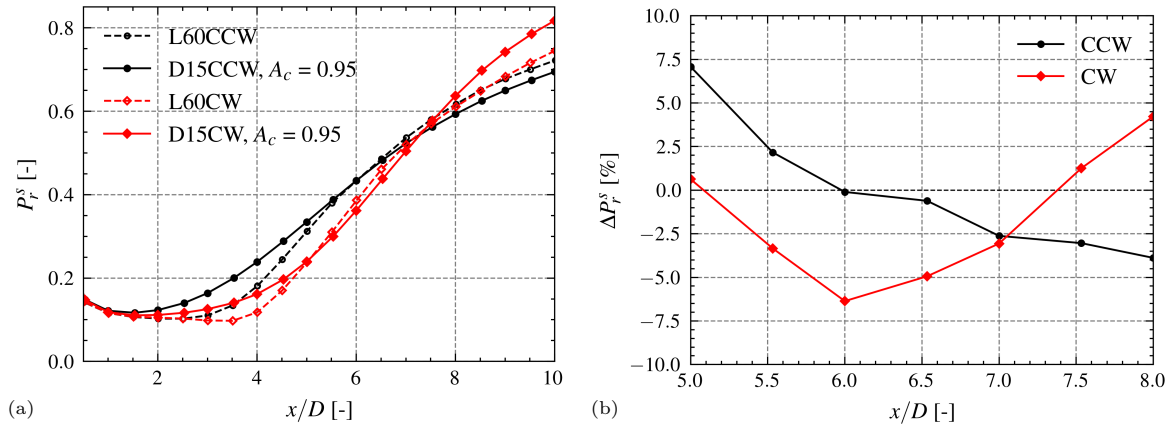

Figure 4.15: The total optimum found for the D15 cases at $A_c = 0.95$. (a) shows the power recovery in the static frame and (b) the corresponding bias between 5D and 8D by comparing to L60 cases.

4.4. Different Strouhal numbers

The dependence of Helix wake recovery on the excitation Strouhal number is an important consideration when optimizing the control method. In the previous sections, Helix wake recovery for a Strouhal number of 0.25 and 0.375 was researched. To further verify the model, the Helix wake recovery for more Strouhal numbers will be tested by comparing the observed behaviour to Cheung et al. (2024). It is relevant to verify specifically the Strouhal dependence since the H-ADM is derived from a $St = 0$ configuration.

Cheung et al. (2024) used an LES solver coupled to OpenFast to research the CCW Helix behaviour at different Strouhal numbers. To quantify this behaviour they applied modal decomposition to the streamwise velocity component, following Citriniti and George (2000). This results in an eigenvalue problem for each streamwise position. The eigenvalues λ_1 represent the turbulent energy at that particular streamwise position. See Cheung et al. (2024) for further details on this computation. The authors found that, for an increasing Strouhal number, the peak of turbulent energy shifts closer towards the

turbine. More specifically, they found for Strouhal numbers 0.375 and 0.45 that the peak occurred around $x/D \approx 4.0$, while a lower Strouhal number 0.225 peaks at $x/D \approx 6.0$. This result suggests that that the frequency of actuation influences the specific downstream position at which wake mixing takes place. Consequently, when the space between turbine is increased, a similar power can be produced on the second turbine by selecting a lower Strouhal number on the first.

To verify that the H-ADM is able to reproduce this Strouhal behaviour, the D30-CCW setup is used with $\alpha = 3.06$ and $A_c = 0.71$ (i.e. the setup used to generate results of Figure 4.11). This setup provides a balance between computation time and accurate results with respect to ALM for the whole wake region, as shown in Figure 4.12. Furthermore, the same Strouhal numbers as in Cheung et al. (2024) will be researched, i.e. $St = 0.225, 0.30, 0.375, 0.45$. To quantify the turbulent energy at each streamwise location, the turbulent kinetic energy (TKE) will be calculated as TKE $= \frac{1}{2}(\langle u'u' \rangle + \langle v'v' \rangle + \langle w'w' \rangle)$, where the primes denote fluctuations around the mean. Again, the averaging time equals five Helix periods. The TKE results are shown in Figure 4.16a. This verifies that the H-ADM is able to capture differences in turbulent energy in the wake as a result of varying Strouhal numbers. An exact agreement with Cheung et al. (2024) is not expected due to gridsize and simulation setup dependence. However, it is interesting to note that initially an exponential increase in TKE is observed, after which saturation occurs. This exponential increase from $x/D \approx 1$ is visible as a linear increase in the log plot of Figure 4.16b. The saturation distance defines the peak of TKE in the wake. Similar to the results of Cheung et al. (2024), this peak occurs earlier for the higher Strouhal numbers (around $x/D = 4.5$) compared to the lower Strouhal numbers (around $x/D = 6$). Figure 4.17 shows this Strouhal effect on the power recovery in the static frame. This verifies that the Strouhal value is important for optimizing the Helix control strategy. If turbines are spaced further apart a lower Strouhal number might be beneficial and vice versa.

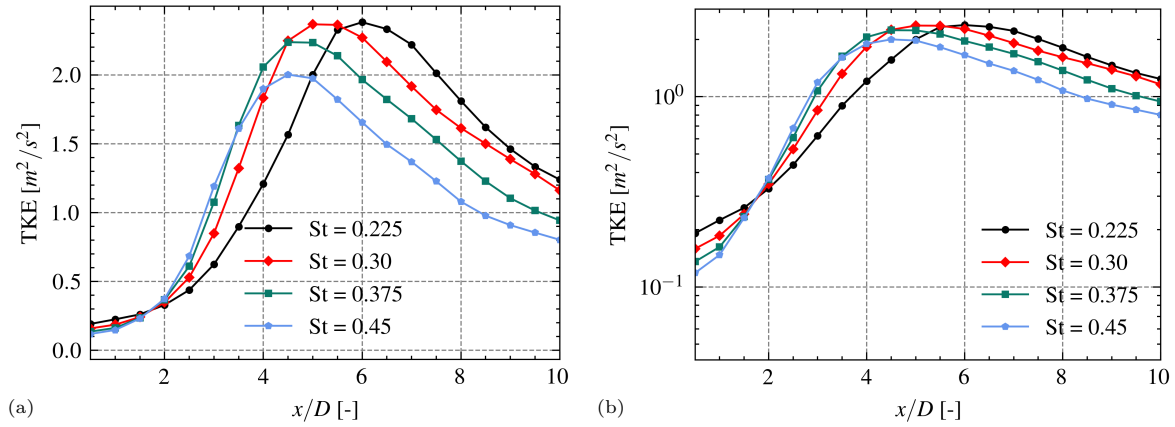

Figure 4.16: Turbulent kinetic energy in the wake at different downstream positions (a). Subfigure (b) shows results on a logarithmic scale, emphasizing the exponential growth.

4.5. Turbulence

After gaining a good understanding of the H-ADM behaviour in laminar conditions, this section aims to extend this by executing simulations with turbulence. This allows us to verify the hypothesis made earlier regarding laminar effects causing the CW divergence and to test differences between Helix turbines and NH turbines. The generation of turbulence is done by using a surface roughness of 0.01 m. The amount of time it takes before the desired TI is reached is referred to as the spin-up time. When averaging results the spin-up time data is not taken into account.

4.5.1. Wake destabilization

As discussed in section 4.2.3, it is hypothesized that the divergence of wake displacement for the CW case might be the result of wake instabilities maintained by laminar inflow. The overestimation has also been observed in the grid-size sensitivity study for coarser resolutions. To research the effects of laminar inflow, the D15 cases resulting from the parameter sweep (i.e. $\alpha = 1.53$ and $A_c = 0.95$) will be simulated with and without turbulence. After the spin-up period of 1200 s, the turbulence intensity at

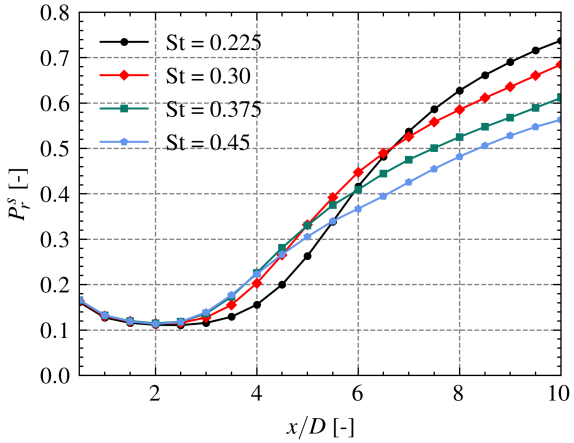

Figure 4.17: The static frame power recovery for different Strouhal numbers.

hub height equals 0.5% (note that the hub is located at z = 720 m). The resulting static frame power recoveries, again averaged over 5 Helix periods, are shown in Figure 4.18a. Figure 4.18b shows the bias, i.e. the difference between the turbulent and laminar simulation expressed as a fraction of the laminar simulation.

Focusing first on the NH simulation it is clear that the additional turbulence enhances the recovery of the wake. In general, turbulence should enhance wake recovery, indicating that the bias should have a positive value. For the CCW case this condition is satisfied for the far wake region ($x/D > 4$). Looking at the CW case an interesting observation is made. Around $x/D = 6$ the positive bias of the CW case drops rapidly, reaching a negative value around $x/D = 8$. This means that the condition of positive bias is not satisfied anymore, indicating that either the laminar case overestimates wake recovery and/or the turbulent case underestimates recovery. It seems reasonable to assume the former to be true, considering the fact that we observe this overestimation of the CW laminar case power recovery for two separate comparisons (i.e. laminar H-ADM to laminar ALM and laminar H-ADM to turbulent H-ADM). A possible explanation could indeed be the wake instabilities involved in laminar simulations. It is important to note that based on this analysis the hypothesis cannot be verified with certainty, but appears reasonable. It seems that the diverging CW behaviour in the far wake is resolved when the inflow is turbulent. Additionally, it would be interesting to gain a further understanding of why only the CW rotating Helix seems affected by this.

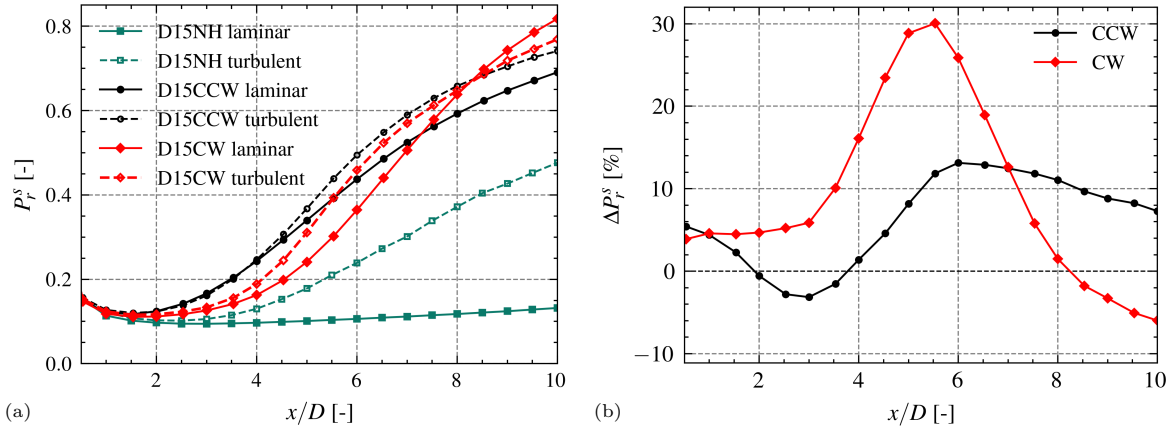

Figure 4.18: The influence of turbulence on the Helix power recovery process (a) and the corresponding bias (b). Laminar corresponds to a TI of 0.0% and turbulent to a TI of 0.5% at hub height.

4.5.2. Turbine power behaviour

So far, the primary focus has been on validating the wake behaviour of the H-ADM. For these simulations the free-stream velocity was known a priori, meaning the thrust and power coefficients were predefined. In verifying and validating the H-ADM we are also interested in knowing how the turbine reacts without predefining coefficients. Specifically, we are interested in figuring out how the turbine's power and thrust are influenced by applying the Helix. For example, Frederik et al. (2020) found a power reduction on Helix turbines of around 1% for specific conditions.

To research this, turbulent simulations are executed with 6 turbines next to each other (i.e. the same x location). These turbines are either all controlled by the CCW Helix, CW Helix or no Helix ("NH"). A spin-up time of 140 min is used. After spin-up the simulation continues for 3 hours, during which the average TI at hub height equals 6.75% and the 10-minute averaged free-stream velocity varies between 8.4 and 9.1 m/s. Contrary to the previous simulations, the turbines are placed at a realistic hub height of z = 150 m. The rotational velocity, coefficient of power and coefficient of thrust are now determined using the rotor performance table from Appendix B. The rotor performance is converted to be a function of the disk averaged velocity as described in Section 2.3.

Figure 4.19 shows the instantaneous power of one NH turbine after the spin-up period. Here the effect of turbulence is clearly visible in the power fluctuations. Comparing this to the result for the CCW and CW turbines, it stands out that the mean power produced by both Helix turbines is approximately 0.4% below the NH power. Upon further inspection it turns out that this is the result of a lower axial disk averaged velocity of the Helix turbines caused by differences in upstream induction. The axial disk averaged velocity u_d of the CCW turbine is 0.14% below u_d of the NH turbine. For the CW turbine u_d is 0.12% below NH. As a result, the thrust force on the Helix turbines decreases as well. On average, the thrust is about 0.27% lower for the CCW turbine and 0.22% lower for the CW turbine. It is interesting that the power loss of the Helix turbine is predicted by the H-ADM without explicitly modelling it. However, it remains unclear whether this difference in induction covers all power losses. Future work should aim to further understand the mechanisms causing the power reductions of Helix turbines and model this with the H-ADM.

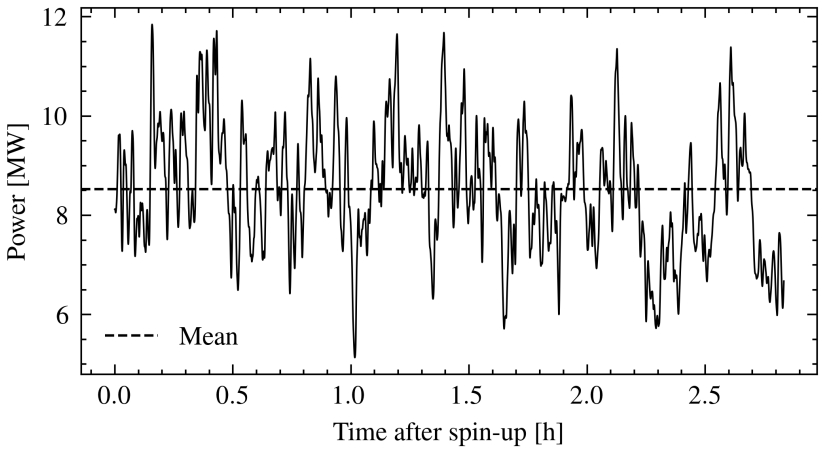

Figure 4.19: Instantaneous power over time for a NH turbine. The dashed line corresponds to the mean power over the considered period.

5

CCW and CW phenomenology

This chapter aims to gain a further understanding of the differences between the CCW and CW Helix. This is achieved by examining the effect the swirling motion of the wake has on the formation of vortices and wake recovery. Section 5.1 researches a non-rotating wake and Section 5.2 investigates the influence of swirl.

5.1. Non-rotating wake

Korb et al. (2023) and Coquelet et al. (2024) have researched ways to gain a better understanding of the Helix wake recovery process. They showed that the Helix wake contains strong vortex structures which enhance the entrainment of kinetic energy into the wake and the displacement of the wake center. Vortical structures in the wake can be quantified by the vorticity field $\boldsymbol{\omega}$, defined as the curl of the velocity field $\mathbf{M}$:

$$\boldsymbol{\omega} = \nabla \times \mathbf{M} = \left(\frac{\partial w}{\partial y} - \frac{\partial v}{\partial z}, \frac{\partial u}{\partial z} - \frac{\partial w}{\partial x}, \frac{\partial v}{\partial x} - \frac{\partial u}{\partial y} \right) \tag{5.1}$$

To research the effect of the swirling wake motion, the rotational force will be turned off in the H-ADM. This means that the wind turbine only exerts a thrust force on the flow, and that the wind turbine force calculated by Equation 3.24 is converted to:

$$\mathbf{f}^{WT}(\mathbf{x},t) = \frac{\mathscr{R}_c^N(\mathbf{x})}{v(\mathbf{x})} \mathscr{H}_n(\mathbf{x},t) F_{n,disk} \mathbf{e}_\perp \tag{5.2}$$

The streamwise vorticity (i.e. ω_x) for the cases D30NH, D30CCW and D30CW without rotational fore, indicated by *casename*-NR, are shown in Figure 5.1. Here the streamwise vorticity is normalized and averaged over 7 Helix periods. For the average, only values corresponding to a certain phase are involved in the calculation. That specific phase is depending on the streamwise position of the considered yz-slice. This approach is described by Coquelet et al. (2024), where in this report the convective speed of the near wake is also assumed to be $0.5u_\infty$. The calculated phase is expressed in terms of the Helix period T_h. Furthermore, the gridsize of the simulations is D/30, but results are interpolated on a grid with a gridsize of D/300 to enhance the readability of the figures. Looking at the results, no vorticity is visible for the NH-NR case at the considered scale since lateral and vertical velocities are very small. On the contrary, for the CCW-NR and CW-NR cases, some vorticity is observed at $x/D = 1$. The azimuthal non-uniformity of the Helix causes additional pressure differences that create more lateral and vertical motions of the flow, resulting in stronger vortex strucutres compared to NH. The chirality of the formed vortex structures is flipped between the CCW and CW cases. Moving further away from the disk to $x/D = 3$, the vorticity is much stronger and additional vortex structures are formed. Again, chirality of the vortices is flipped, but other than that the structures appear similar. We observe counter rotating vortex pairs (CVP) in the center and towards the edge of the wake, similar to what was found by Gutknecht et al. (2023) and Coquelet et al. (2024). The CVPs are known to deflect the wake from its center position (Howland et al., 2016). An initial displacement from the center is already visible in the vorticity plots at $x/D = 3$ for both Helix cases. Quickly after $x/D = 3$, the wake gets more turbulent and the individual vortex structures cannot be distinguished anymore.

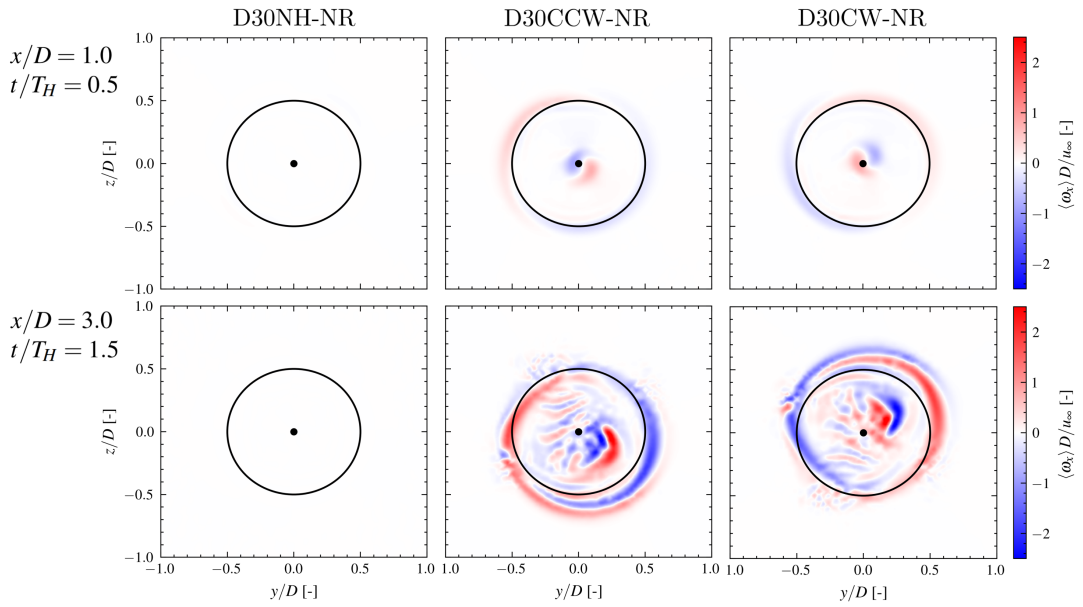

Figure 5.1: The streamwise vorticity at different streamwise positions (rows) and H-ADM configurations without rotational force (columns). The line of sight is downstream. The rotor area is indicated by the black circle and the dot corresponds to its center.

It is of interest to find out what the effect of the similar vortex structures observed for the Helix NR cases is on the wake recovery process. To research this, the static frame power recovery for the Helix cases with and without rotation are shown in Figure 5.2. Remarkably, the similarity in vortex structure between CCW-NR and CW-NR translates directly to a similar wake recovery. This shows that the swirl of the wake is responsible for the difference between the CW and CCW Helix.

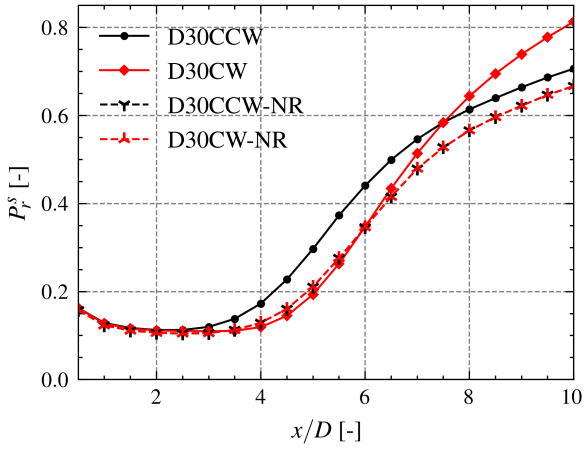

Figure 5.2: The static frame power recovery for the CW and CCW Helix configurations. The suffix ”-NR” corresponds to the simulations without rotational force.

5.2. The influence of swirl

It is clear that the swirl in the wake causes the difference in wake recovery between the CW and CCW Helix. To further understand this, the streamwise vorticity for the D30NH, D30CW and D30CCW cases is shown in Figure 5.3 (i.e. now including rotational force). Similar to Coquelet et al. (2024) the NH case creates vorticity in the positive (CW) direction at the outer edge of the wake and the negative direction (CCW) near the hub. This is the result of the rotational force gradient near the edge and center of the disk, as defined by the radial correction function of Figure 3.4. Due to laminar

inflow, the NH wake is stable. This is visible when looking at the streamwise vorticity at $x/D = 3$ where no additional vortex structures are created compared to $x/D = 1$. Looking at the Helix cases, it is important to note that the rotation direction of the wake and the Helix are similar for the CCW Helix and opposite for the CW Helix. At $x/D = 1$ a difference between the CW and CCW case stands out immediately. The negatively rotating vortex seems to be stronger and displaced from the center for the D30CW case, where a positively rotating vortex is induced. An interesting observation can be made when comparing the Helix cases at $x/D = 3$ to the NR Helix cases. It appears that for the D30CCW case, the inner CVP has reduced in strength as a result of the swirling wake motion and that the outer CVP strength has increased. For the D30CW case the opposite can be observed, where the inner CVP appears stronger and the outer CVP appears weaker compared to the D30CW-NR case. This difference in dominant CVP structure might explain the difference between the effectiveness of the CW and CCW Helix. The outer CVP might be more efficient in displacing the wake and/or mixing higher energy ambient air into the wake. However, the inner CVP might be more stable due to its positioning, which could explain why the CW Helix eventually catches up with the CCW Helix in terms of wake recovery. It is important to remember that the H-ADM does not account for detailed flow phenomena, such as the hub vortex. Therefore, it should be kept in mind this could influence the results we observe here.

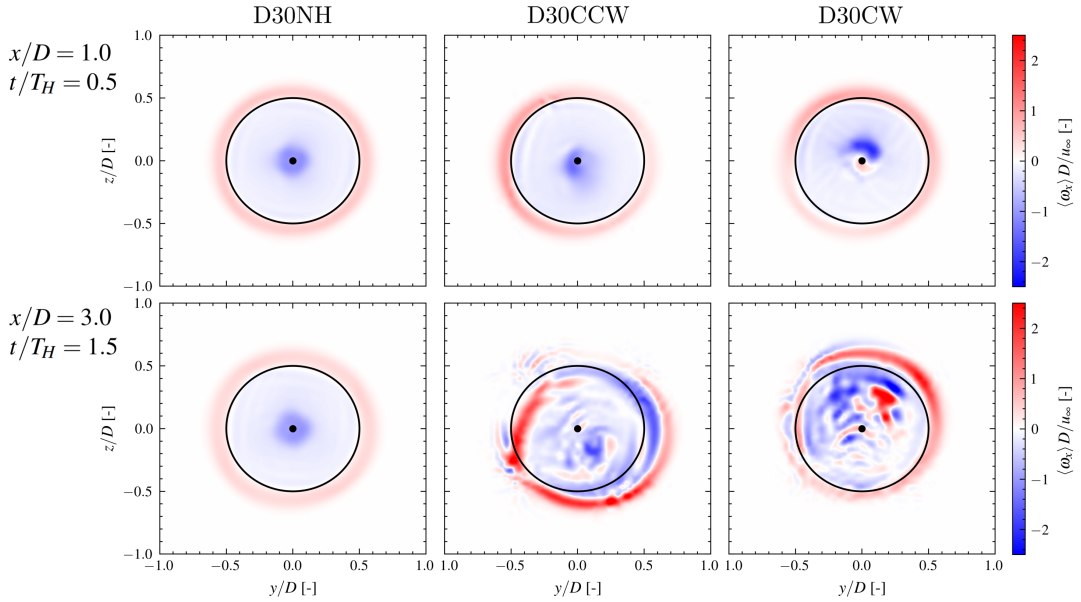

Figure 5.3: The streamwise vorticity at different streamwise positions (rows) and Helix configurations (columns). The line of sight is downstream. The rotor area is indicated by the black circle and the dot corresponds to its center.

To quantify the difference in vorticity, the circulation Γ will be calculated. The circulation is defined as the line integral over a closed loop of the velocity field. Using Stokes' theorem this can be rewritten to:

$$\Gamma = \oint_{\partial S} \mathbf{M} \cdot \mathrm{d}\mathbf{l} = \iint_S \nabla \times \mathbf{M} \cdot \mathrm{d}\mathbf{S} = \iint_S \boldsymbol{\omega} \cdot \mathrm{d}\mathbf{S} \tag{5.3}$$

with ∂S the boundary of surface S. Results of the circulation at $x/D = 3$ with $\mathrm{d}\hat{\mathbf{S}} = (1,0,0)$ and integration domain $y_{hub} - D < y < y_{hub} + D$, $z_{hub} - D < z < z_{hub} + D$ are shown in Table 5.1. Here the circulation is split between Γ^+, with only positive contributions of $\boldsymbol{\omega}_x$, and Γ^-, with only negative contributions of $\boldsymbol{\omega}_x$, and $\Gamma = \Gamma^+ - \Gamma^-$. Additionally, the integration is divided in circulation within the rotor disk, denoted by subscript "in", and outside the rotor disk, denoted by subscript "out". Looking at the results, it is immediately clear that the positive and negative circulation components are larger for the Helix cases. This aligns with observations from Figures 5.1 and 5.3. However, it is surprising that there is a difference in Γ^+ and Γ^- between the CCW-NR and CW-NR cases. If no rotational force is exerted by the turbine, the CW and CCW case are not expected to react differently to the incoming laminar flow. The difference in vorticity magnitude between CW and CCW is amplified when rotation is turned on, indicating that the vortex structures get even stronger for CCW compard to CW under the influence of swirl. For all cases, the postive vorticity is balanced by negative vorticity, meaning that the total

Table 5.1: Circulation for the different cases at $x/D = 3$.

	$\Gamma^+/(Du_\infty)$ [-]	$\Gamma^-/(Du_\infty)$ [-]	Γ^+_{in}/Γ^+	Γ^+_{out}/Γ^+	Γ^-_{in}/Γ^-	Γ^-_{out}/Γ^-	Γ_{out}/Γ_{in}
NH-NR	0.1	0.1	0.45	0.55	0.45	0.55	1.24
CCW-NR	8.5	8.5	0.54	0.46	0.42	0.58	1.08
CW-NR	8.2	8.2	0.42	0.58	0.54	0.46	1.09
NH	4.4	4.4	0.01	0.99	1.00	0.00	0.97
CCW	10.0	10.0	0.30	0.70	0.60	0.40	1.23
CW	9.3	9.3	0.29	0.71	0.85	0.15	0.75

circulation is zero. Interestingly, the effect of swirl is that the share of Γ^+ outside of the rotor area increases for all cases. This indicates that the positive vorticity is transferred outwards away from the rotor axis as a result of swirl. The opposite appears to be the case for Γ^-. Here the fraction within the rotor area increases as a result of swirl, meaning that the negative vorticity will be contained within the rotor area. The final column, Γ_{out}/Γ_{in}, is calculated as $(\Gamma^+_{out}+\Gamma^-_{out})/(\Gamma^+_{in}+\Gamma^-_{in})$. This means it reflects the absolute circulation outside the rotor area as a fraction of the absolute circulation inside it. Without swirl, both Helix configurations have a ratio higher than 1, i.e. the circulation is more concentrated outside of the rotor disk area. Now, when swirl is enabled the ratio for CCW increases. This indicates that the vortical structures outside the rotor disk get even more dominant. For CW the contrary is observed, where the ratio decreases and vortical structures on the inside of the rotor strengthen. These observations align with the hypotheses made earlier this section. The increased ratio for the CCW case could be caused by the amplification of the outer CVP, whereas the decreased ratio for the CW case could be caused by the amplification of the inner CVP.

6

Application to a wind farm

This chapter applies the verified and validated H-ADM on a farm-size scale, thereby leveraging the computational advantages of the ADM over the ALM. Section 6.1 discusses the simulation setup used. Then, Section 6.2 shows the results for Helix actuation on the first row of turbines. Section 6.3 looks at the effect of Helix turbines deeper in the farm. Finally, Section 6.4 investigates the effect of Helix synchronization.

6.1. Farm setup

The considered wind farm has an aligned pattern of 8 rows by 6 columns. The turbines are spaced 6D apart in both the streamwise and lateral direction. The simulated domain dimensions are 15,360 m in streamwise direction, 8,640 m in lateral direction and 2,400 m in vertical direction. The domain is discretized by a grid-size of D/15, resulting in a grid of 960x540x150 cells. The first and last 30 cells of the domain in streamwise direction are used for nudging. All turbines again model the IEA 15MW reference turbine, with a diameter D of 240 m, hub height of 150 m and rotor performance as documented in Appendix B. The rotor performance is converted to be a function of the disk averaged velocity as discussed in Section 2.3. To generate realistic ABL conditions, turbulence is generated by setting a surface roughness of 0.01 m. A spin-up time of 140 min is chosen, after which the wind farm results are averaged over 3 hours. This means that u_∞ varies between 8.4 and 9.1 m/s and the average hub height TI is around 6.75%. The turbulence and wind velocity development over time are further discussed in Appendix C. An instantaneous overview of the farm with CCW Helix turbines on the first row is shown in Figure 6.1.

6.2. Helix turbines on the first row

The baseline case ("NH") simulates the farm with all 48 turbines operating under standard conditions. Then, to research the Helix effect on large scale, the first row of wind turbines is controlled by the CW Helix ("CW") or CCW Helix ("CCW") with all other turbines under standard conditions again. The large scale effect of the Helix will be studied for $St = 0.25$ and $A = 2.5°$. The amplitude correction factor A_c resulting from the parameter sweep will be used, i.e. $A_c = 0.95$. The effect of the Helix will be assessed by studying the power production averaged over time. As a first step, the average power production of each row is shown in Figure 6.2. Here, the power is normalized by the average power of the first row of the NH simulation P_0. In the first row a power difference of 0.4% is observed between no Helix and Helix turbines, identical to what was discussed in Section 4.5.2. Since this power loss is not validated and fully understood, it is decided to focus on the power gains of turbines deeper in the farm that operate under standard conditions.

The second row experiences power gains for both Helix simulations. The CCW simulation sees a gain of +22.6% and for the CW simulation a gain of +8.3% is observed. Comparing to the results of Frederik et al. (2020) these numbers seem to match expectations, where the reduction of thrust of the Helix turbines could indicate that we slightly overestimate the power production of the second row. Interestingly, the third row still experiences power gains for both Helix simulations; +0.5% for CCW and +2.6% for CW. This is not a trivial result. Since the power increases on the second row turbines,

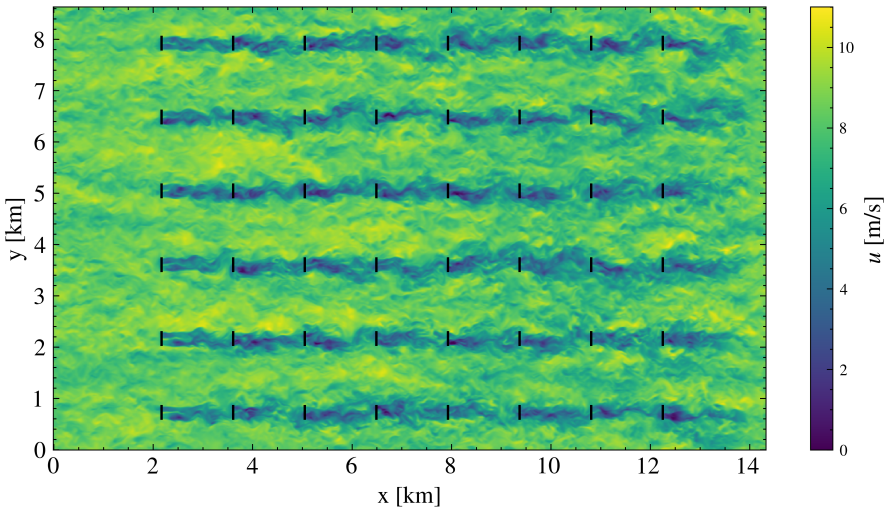

Figure 6.1: An instantaneous visualization of the CCW wind farm. Each black line corresponds to a turbine. The IEA 15MW reference turbines are spaced 6D apart in streamwise and lateral direction. In the last 30 gridcells of the domain the nudging zone is visible.

these turbines also exert a higher thrust force (+11.6% for CCW and +4.3% for CW on average). Apparently, the higher wake velocity at the second turbine compensates for the higher thrust, resulting in still more energy available for the third row turbines. Additionally, it is interesting to note that the CW Helix seems to outperform the CCW Helix on the third row. Going even deeper into the farm, the power gains start to decrease, going below 0 to -3.1% for CCW and -2.8% for CW. From the sixth row onwards the negative power gains for the Helix cases seem to recover slowly back to 0%. The total farm power gains (excluding the Helix turbines since power reduction is not verified) equal +1.5% for CCW and +0.2% for CW.

To further understand the behaviour deeper in the wind farm, simulation slices through the turbine hubs are shown in Figure 6.3. Here the data is averaged over time and all columns. For the Helix cases, differences with respect to the NH simulation are shown. The axial velocity horizontal slice (Figure 6.3a) shows what we have seen before; the Helix simulations recover quicker than NH, and CCW even faster than CW. Remarkable is the large axial velocity decrease for the CW Helix at the location of the hub jet, also observed in Figure 4.5. Axial velocity gains are observed after the second row for both Helices and diminish after the third. Towards the end of the farm we again observe regions of velocity gains in the turbine arrays. This all translates to the power gains we have seen in Figure 6.2. A remarkable result is that, especially for the CW Helix, regions of positive axial velocity gain seem to travel sideways

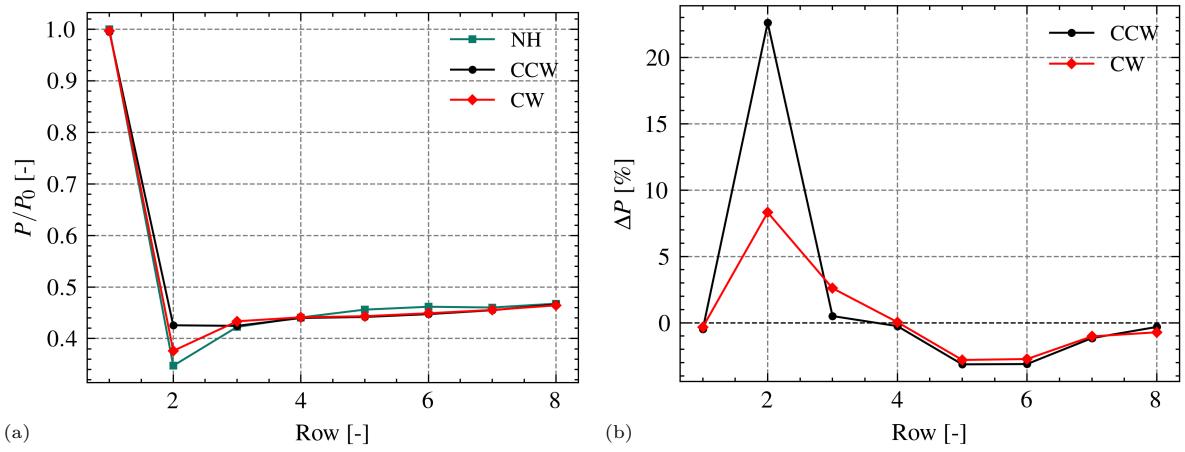

Figure 6.2: The time averaged power production averaged per row of the wind farm (a) and the gain of the Helix simulations with respect to the NH simulation (b).

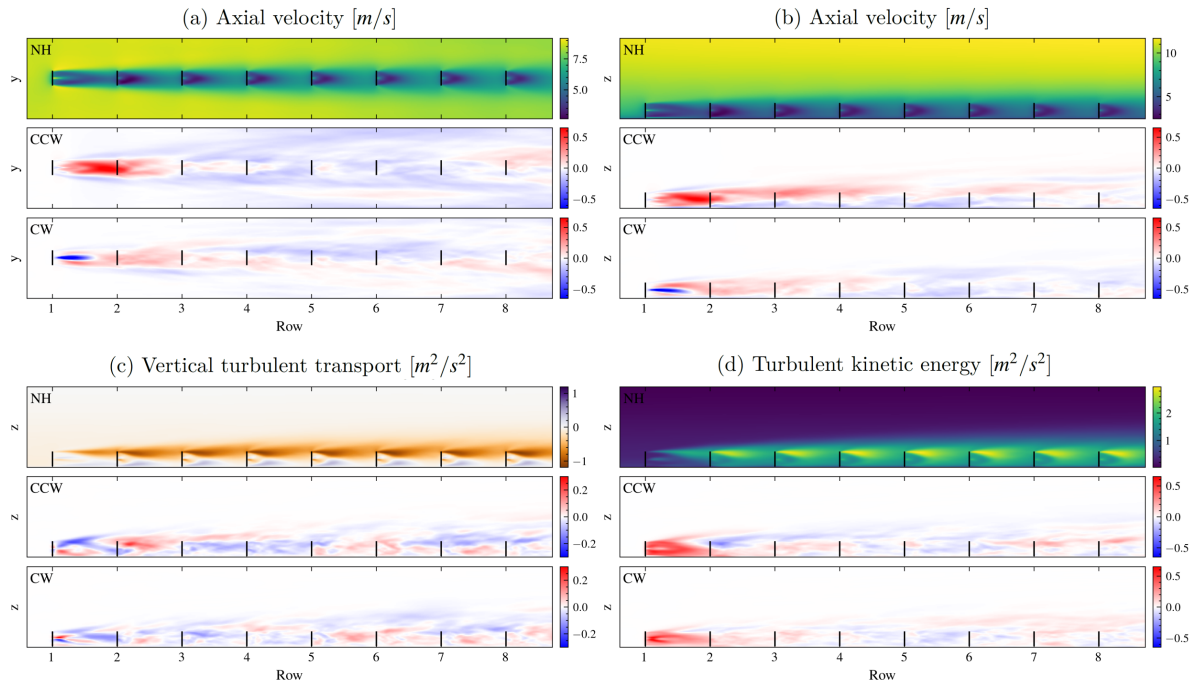

Figure 6.3: Column averaged slices of flow field data through the turbine hubs. Top figure of each subfigure corresponds to the NH simulation, the second figure to CCW and the third to CW. The CCW and CW figures show the difference with respect to the NH figure. The vertical turbulent transport is defined as $\langle u'w' \rangle$ and turbulent kinetic energy TKE as $(\langle u'u' \rangle + \langle v'v' \rangle + \langle w'w' \rangle)/2$.

away from the turbine arrays. This could provide a possible explanation for the reduction of Helix power gains observed deeper in the farm. Compared to the pulse method studied by Munters and Meyers (2018), it is notable that in their case the increases in axial velocity is maintained within the wake region throughout the farm. In Figure 6.3b a similar effect but in vertical direction is observed. The axial velocity gains start spreading upwards deeper into the boundary layer. Looking at Figure 6.3c, negative values of vertical turbulent transport at the top of the wakes are observed for the NH simulation. This indicates that momentum is transported downwards into the wake. On the contrary, a positive vertical turbulent transport corresponds to transport of momentum in positive z direction. For the Helix cases the bottom parts of the Helix wakes experience increased upward transport of momentum, whereas the top parts of the wakes experience increased amounts of downward transport of momentum. Both deviations are beneficial for wake mixing. However, for the CCW simulation the opposite occurs at the top of the wake of the second row. The turbulent transport value increases meaning that less momentum is transported into the wake. This could explain the decrease of power gains at the third row. For the CW simulation this effect is not observed in the wake of the second row, which could explain why CW outperforms CCW on the third row. Towards the end of the domain we again observe positive gains of turbulent transport into the wake. This could explain the recovery of power gains towards the end of the domain as observed in Figure 6.2. Figure 6.3d shows that both the CCW and CW Helix wakes contain increased amounts of TKE. Similar to the other studied metrics, we mainly observe regions of gains in the beginning and towards the end of the farm. In the middle of the farm, between row 4 and 6, we observe a decrease in TKE contributing to the explanation of negative power gains observed in Figure 6.2.

6.3. The effect of Helix turbines deeper in the farm

Last section showed that Helix actuation on the first row of turbines has the potential to increase the total power production of the considered wind farm. For this particular wind farm, the CCW Helix showed larger overall gains than the CW Helix. For both configurations, the power gains seem to diminish after the third row. Naturally the question arises if we can increase the total power production by Helix actuation of turbines deeper in the farm. That question will be addressed in this section. To do

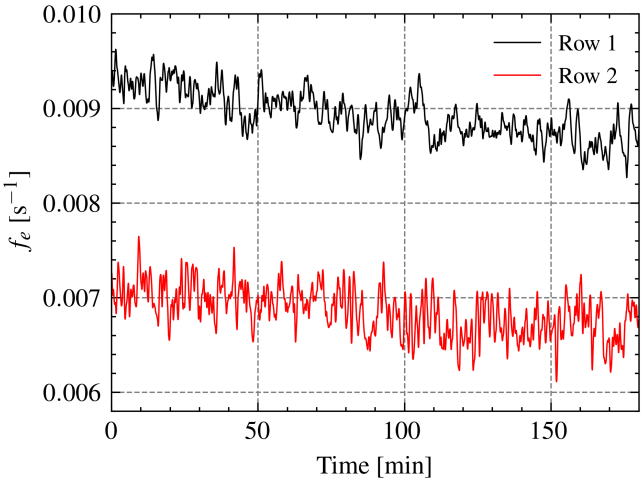

Figure 6.4: Instantaneous Helix frequencies f_e over time for turbines on row 1 and row 2. Results are averaged over all turbines of each row.

so, the same farm layout as before will be used where the first row of turbines will be controlled by the CCW Helix. Then, one additional row deeper within the farm will contain turbines controlled by the CCW Helix as well. All Helix turbines start at a phase of 0° and will operate independent of each other to maintain $St = 0.25$. To realize this, the disk averaged velocity of each turbine is calculated at each time-step. Using the prime curve routine of Section 2.3, we can calculate the corresponding free-stream velocity. The resulting turbine specific free-stream velocity is used to calculate the excitation frequency required to achieve a Strouhal number of 0.25. Over time, this results in varying phase offsets between the Helix turbines.

As a first step, the additional row of CCW turbines is the second row. This means that now the first two rows of the wind farm contain CCW Helix turbines. This simulation case is referred to as "CCW2". The different Helix frequencies between the first and second row turbines, caused by a constant Strouhal number for all turbines, are shown in Figure 6.4. Turbines on the second row require a lower Helix frequency to maintain $St = 0.25$. This is the result of the wakes of turbines on row one, which cause row two turbines to experience a reduced free-stream velocity. The power gain of CCW2 with respect to CCW is shown in Figure 6.5. Again, power losses on the Helix turbines are observed. On the second row this amounts to an average loss of 0.7%. A power increase on the third row is observed as a result of Helix actuation in the second row. However, the gains are much lower than before at +1.9%. Then, similar to earlier observations the power gains diminish. This results in negative gains of almost 1%. Interestingly, the power seems to recover again towards the end of the domain, ultimately resulting in

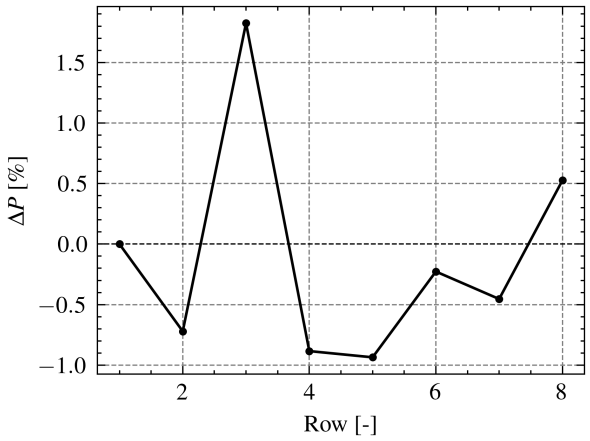

Figure 6.5: The power gain of additional Helix turbines in the second row of the wind farm.

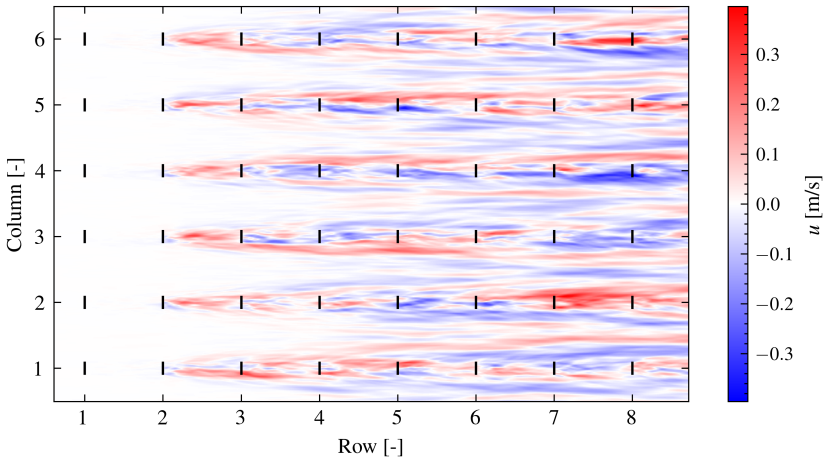

Figure 6.6: The axial velocity gain for the CCW2 farm with respect to the CCW farm.

positive gains. The time averaged axial velocity difference throughout the farm with respect to the CCW case is shown in Figure 6.6. Again, we observe that regions with higher axial velocities travel away from the wind turbine arrays. The total time averaged power gain compared to the CCW case amounts to -0.02% for the non-Helix turbines (i.e. row $>$ 2).

To research the effect of Helix turbines even deeper in the farm, simulations are analyzed with the additional CCW turbines on row 3. This means we consider a farm with Helix turbines on row 1 and 3, i.e. "CCW3". The Helix turbines operate similarly as before, where $St = 0.25$ is forced and the frequencies f_e will vary mutually as a result. The power gains of CCW3 compared to CCW are shown in Figure 6.7. Again, the Helix turbine experiences a power loss of almost 0.7% as a result of differences in upstream induction. Power increases by almost 3.0% on the fourth row due to Helix actuation on the third. Interestingly, this is a larger gain compared to the CCW2 case, where only +1.9% was observed. Similar to earlier observations, the power gains diminish rapidly leading to negative gains. Towards the end of the domain the power recovers. The overall power gains for the farm excluding Helix turbines equals 0.0%. This means that for the considered wind farm layout power gains of additional Helix actuation deeper in the farm (row 2 or 3) do not compensate for the Helix losses.

It should be noted that the reliability and stability of these results remains unclear. For example, the boundary layer is still transient after the spin-up period. Also, the influence of domain size and nudging settings have not been researched extensively due to time constraints. One could argue that these factors are similar for the different simulations, meaning that results could be compared mutually. That is probably true for the CCW, CW and NH farms, since we apply a perturbation at only the

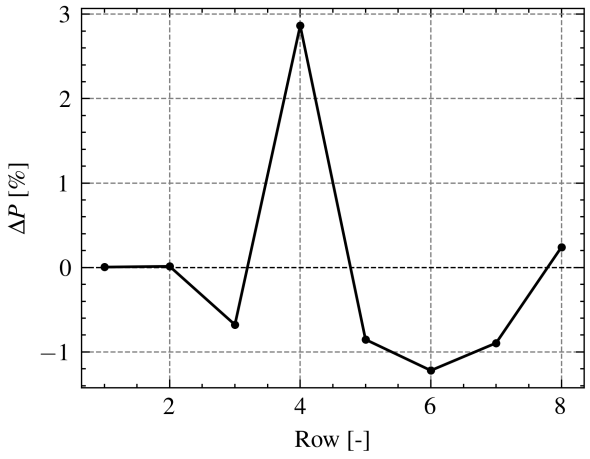

Figure 6.7: The power gain of additional Helix turbines in the third row of the wind farm.

first row in each case. However, we should be extra careful when comparing them to simulations with perturbations deeper in the farm. These deeper perturbations lead to different dynamics introducing additional uncertainty.

6.4. Synchronization

Korb et al. (2023) have shown that the phase offset between two consecutive rows of Helix turbines is an important consideration for optimizing the control approach. The main idea is to maintain a constant offset between the phase of the Helix wake arriving at the second row Helix turbine, and the phase of the second row turbine Helix. This approach is called Helix synchronization. In practice, this is not a trivial task. For example, in our farm simulation we are dealing with an inflow velocity that is slowing down over time. Korb et al. (2023) demonstrated that this significantly alters the speed at which the Helix is conveyed to the turbines in the second row. As a result, it is very difficult to accurately estimate this Helix transport velocity a priori. However, knowing the Helix transport velocity is essential to calculate the required Helix phase on the second row turbine for the desired phase offset.

It is clear that advanced procedures are required to apply synchronization in our wind farm simulation. Due to time constraints we have to omit this. However, we can still research the potential of Helix synchronization by setting a constant phase offset between the Helix turbines on the first and second row. This means we will again consider the CCW2 case, but now the phase difference between the two rows is predefined. All Helix turbines on the first row start at a Helix phase of 0°. The second row turbines are initialized with a Helix phase equal to the desired synchronization phase offset. The researched phase offsets are 0°, 90°, 180° and 270°. The first row turbines operate at $St = 0.25$ and the second row turbines have a frequency equal to the turbine directly in front. This means the Strouhal number varies between the two Helix rows as they experience different free-stream velocities. This effect is shown in Figure 6.8.

Results of the constant phase offset simulations are shown in Figure 6.9. This figure visualizes the power gains on the third row with respect to the CCW case, i.e. only Helix actuation on the first row. Immediately, it is clear that the effectiveness is angle dependent. This is in agreement with observations from Korb et al. (2023). Results also reveal that the Helix effect of accelerated wake recovery can be maintained until the third row by synchronization, yielding a power gain of almost 3.4% for a phase offset of 270°. Before, without the constant phase offset, a power gain of only 1.8% was found in the third row as shown in Figure 6.5.

It should be noted again that the Helix transport velocity varied over time. We did not correct for this, meaning that the offset between Helices at the second row also varied. Therefore, this analysis mainly serves to show that the H-ADM can capture synchronization effects and that Helix synchronization has the potential to carry Helix gains deeper into the farm. Interesting future research would be

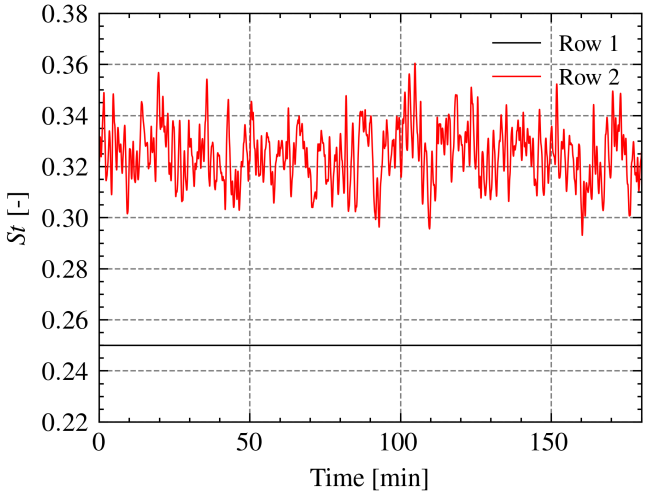

Figure 6.8: Instantaneous Strouhal numbers St over time for turbines on row 1 and row 2. Results are averaged over all turbines of each row.

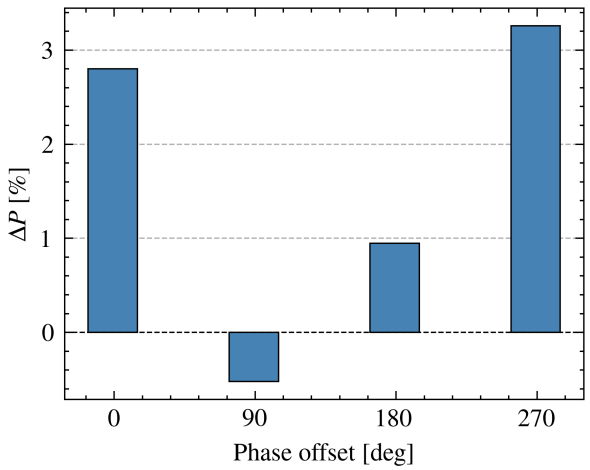

Figure 6.9: The results of a constant phase offset between Helix turbines on the first and second row. The figure shows power gains of the third row compared to a CCW Helix on just the first row.

to analyze the velocity field data from these simulations. From this, the Helix transport velocity can be calculated. Consequently, the real Helix phase offset that occurred in the simulation can be calculated as a function of time. This could provide more insights on the optimal settings of Helix synchronization and potential gains.

7

Conclusion

The main objective of this work is to create an ADM that can simulate the Helix control approach. Modelling the Helix this way allows for faster simulations than current state of the art. Consequently, after verification and validation of the developed model, additional research goals are to apply the Helix control approach on a larger scale and to further understand the underlying mechanisms causing the difference between the CCW and CW Helix.

The H-ADM is derived by treating the Helix as a perturbation to the force distribution over the rotor area. The shape of this force distribution is determined using BE theory. As a result, radial profiles of the lift slope and chord length are additional turbine dependent inputs of the model compared to the U-ADM. As a first step in validating the model, the H-ADM wake recovery is compared to the ALM at an equal resolution and in laminar inflow of 9 m/s. The investigated domain stretches from 0 to 10 turbine diameters behind the turbine. The ALM overestimates turbine forces compared to the H-ADM. As a result, the H-ADM power recovery for the no Helix turbine has a large initial bias compared to ALM, but this bias decreases to below +7.5% after $x/D = 4$. It should be noted that the bias is expected to decrease even further for turbulent simulations. For the CCW Helix with $A = 2^\circ$ and $St = 0.25$, the H-ADM accurately simulates the wake recovery where the absolute power recovery bias stays below 5% from $x/D = 4$ onwards. By accurate it is meant that the absolute power recovery bias is below the no Helix simulation bias. For the CW Helix diverging behaviour towards the end of the domain is observed. Further examination reveals this is due to an overestimation of the wake displacement. It is hypothesized this could be the effect of instabilities in the wake vortex structure that are maintained by laminar inflow. To verify this, similar simulations are executed but now with a TI of 0.5%. Here the divergence of the CW Helix wake mixing and displacement disappeared. Additionally, the H-ADM is verified for different model conditions. Its performance is examined for a different free-stream velocity $u_\infty = 7m/s$, different Helix amplitude $A = 1^\circ$ and different Strouhal number $St = 0.375$. Results show the H-ADM is able to adapt to different model parameters with an absolute power recovery bias below 7.5% from 5D onwards for all cases.

Next, the H-ADM wake recovery at a coarser resolution is examined. It turns out that the force gradient resulting from the Gaussian spreading has a large influence on the results. Keeping the force gradient constant for different resolutions achieves more accurate results than a constant spreading parameter α. By reducing the resolution to 15 points per turbine diameter, instead of 60 for the ALM, the H-ADM proves to be over 640 times faster than the ALM for a slightly larger domain. The mean absolute power bias between 5D and 8D is around 12%. A parameter sweep at this coarse resolution is carried out decreasing the mean power bias to 3.1%. Additionally, non-zero Strouhal behaviour of the H-ADM is verified. This reveals that the H-ADM reproduces effects observed for different Strouhal numbers, such as earlier mixing for a higher Strouhal number.

As a final step in verifying and validating the model, the power and thrust of the Helix turbine itself is researched. Literature shows that a reduction in power could be expected. However, power reduction on the Helix turbine itself is not explicitly modelled by the H-ADM. Results reveal that the upstream induction of Helix turbines differs from no Helix turbines. Consequently, the power production of the CCW and CW Helix turbines is 0.4% below a no Helix turbine. This indicates that parts of the power reduction of Helix turbines could potentially be attributed to upstream induction. Future research

should focus on the mechanisms causing power losses of Helix turbines and ways to model this in the H-ADM framework.

After gaining an understanding of the H-ADM performance, the model is used to research the underlying phenomenology of the CCW and CW Helix. The rotational force in the H-ADM is turned off and vortical structures are examined. This shows that the wake recovery difference between CCW and CW is caused by the rotational force. Analysis of vortical structures reveals that the CCW Helix amplifies the outer CVP, whereas the CW Helix amplifies the inner CVP. This difference in dominant vortex structure could explain the difference in wake recovery observed for the two configurations.

Finally, the H-ADM is used to simulate the Helix on a larger scale. This research considers a wind farm with 48 turbines divided between 8 rows and 6 columns with a spacing of 6D in streamwise and lateral direction. The first row of turbines was actuated by either no Helix, a CCW Helix or CW Helix. Similar to literature, power gains on the second row were observed for both Helices compared to no Helix; +22.6% for CCW and +8.3% for CW. Surprisingly, the CW Helix outperformed the CCW Helix on the third row, with +0.5% for CCW and +2.6% for CW. Deeper into the farm power gains start to diminish even becoming negative. The total power gains of the farm excluding Helix turbines amounted to +1.5% for CCW and +0.2% for CW compared to no Helix actuation on the first row. Actuation of turbines with a Helix deeper in the farm does not lead to significant power gains if a fixed Strouhal number is applied. However, synchronizing the Helix phases of two consecutive Helix turbines by a constant offset succeeds in carrying Helix power gains deeper into the farm. Due to time constraints, the stability of farm results could not be researched further. Therefore results can be compared mutually, but could be off individually. Additionally, to assess the overall power gains of the wind farm using the Helix it would be crucial to accurately model power losses of Helix turbines with the H-ADM.

8

Recommendations

This chapter discusses ways to improve and further validate the current H-ADM. It is chosen to specifically focus on the model and omit discussions on its usage. Below, five points for future research are addressed in no particular order.

- The H-ADM is designed to operate independently of detailed airfoil look-up tables. One of the reasons for this modelling decision is that this could enable the model to be applicable to different turbines. For the IEA 15MW reference turbine the detailed blade information is available. This enables us to obtain the exact radial input profiles needed for the H-ADM. Still a correction factor is required. Interesting future research would be to explore if omitting detailed airfoil tables indeed allows for a general applicability of the H-ADM. For instance, examining the model sensitivity for varying distributions of normalized chord length and lift slope could serve as a starting point.
- The H-ADM is verified for different atmospheric conditions and model parameters. For the considered cases the model kept performing well without requiring changes to the amplitude correction factor. Since the correction factor accounts for unsteady aerodynamics and the underestimation of turbine forces by the H-ADM, a constant correction factor for different conditions could mean two things: (i) the unsteady aerodynamics and force underestimation do not change or (ii) the unsteady aerodynamics and force underestimation do change but the differences cancel each other out. It seems reasonable that both explanations will fail for more extreme conditions, such as higher wind speeds or Strouhal numbers. Therefore, it would be interesting future research to extend the range of researched model parameters.
- The H-ADM wake recovery is validated in laminar conditions to the ALM. In these conditions the wake recovery depends entirely on the turbine model. Turbulence is a wake mixing mechanism independent of the turbine model. Therefore, it is expected that the wake recovery differences between the two models decreases in turbulent conditions. Interesting future research would be to verify this hypothesis by validating the H-ADM to the ALM in turbulent inflow. Additionally, this could verify the hypothesis that the CW Helix divergence is the result of maintained wake instabilities in laminar flow.
- The H-ADM significantly decreases computation time compared to the ALM. Additional computational gains are achieved by increasing the grid-size. However, this research showed the importance of a constant force gradient that limits the maximum possible grid-size. It would be interesting future research to test these limitations by examining coarser resolutions and different force gradients.
- The current research has focused on accurately simulating the Helix wake recovery in an ADM framework. To asses the total power gains of a wind farm with Helix control, it is crucial to accurately model the power losses of the Helix turbines as well. This research reveals that a part of Helix turbine power losses may be attributed to upstream induction. It would be interesting future research to further understand the underlying mechanisms causing the power reductions and model these into the H-ADM.

References

Andersson, L. E., Anaya-Lara, O., Tande, J. O., Merz, K. O., & Imsland, L. (2021). Wind farm control - part i: A review on control system concepts and structures. IET Renewable Power Generation, 15(10), 2085–2108. https://doi.org/https://doi.org/10.1049/rpg2.12160

Baas, P., Verzijlbergh, R., Dorp, P. V., & Jonker, H. (2022). Investigating energy production and wake losses of multi-gigawatt offshore wind farms with atmospheric large-eddy simulation. https://doi.org/10.5194/wes-2022-116

Barthelmie, R. J., Pryor, S. C., Frandsen, S. T., Hansen, K. S., Schepers, J. G., Rados, K., Schlez, W., Neubert, A., Jensen, L. E., & Neckelmann, S. (2010). Quantifying the impact of wind turbine wakes on power output at offshore wind farms. Journal of Atmospheric and Oceanic Technology, 27, 1302–1317. https://doi.org/10.1175/2010JTECHA1398.1

Bir, G. (2008). Multiblade coordinate transformation and its application to wind turbine analysis: Preprint. http://www.osti.gov/bridge

Böing, S. J., Jonker, H. J., Siebesma, A. P., & Grabowski, W. W. (2012). Influence of the subcloud layer on the development of a deep convective ensemble. Journal of the Atmospheric Sciences, 69, 2682–2698. https://doi.org/10.1175/JAS-D-11-0317.1

Burton, Sharpe, Jenkins, & Bossanyi. (2001). Wind energy handbook.

Calaf, M., Meneveau, C., & Meyers, J. (2010). Large eddy simulation study of fully developed wind-turbine array boundary layers. Physics of Fluids, 22. https://doi.org/10.1063/1.3291077

Cheung, L. C., Brown, K. A., Houck, D. R., & deVelder, N. B. (2024). Fluid-dynamic mechanisms underlying wind turbine wake control with strouhal-timed actuation. Energies, 17. https://doi.org/10.3390/en17040865

Citriniti, J. H., & George, W. K. (2000). Reconstruction of the global velocity field in the axisymmetric mixing layer utilizing the proper orthogonal decomposition. Journal of Fluid Mechanics, 418, 137–166. https://doi.org/10.1017/S0022112000001087

Coquelet, M., Gutknecht, J., Wingerden, J. W. V., Duponcheel, M., & Chatelain, P. (2024). Dynamic individual pitch control for wake mitigation: Why does the helix handedness in the wake matter?

Coquelet, M., Moens, M., Duponcheel, M., Wingerden, J. W. V., Bricteux, L., & Chatelain, P. (2023). Simulating the helix wake within an actuator disk framework: Verification against discrete-blade type simulations. Journal of Physics: Conference Series, 2505. https://doi.org/10.1088/1742-6596/2505/1/012017

Frederik, J. A., Doekemeijer, B. M., Mulders, S. P., & van Wingerden, J. W. (2020). The helix approach: Using dynamic individual pitch control to enhance wake mixing in wind farms. Wind Energy, 23, 1739–1751. https://doi.org/10.1002/we.2513

Frederik, J. A., & van Wingerden, J. W. (2022). On the load impact of dynamic wind farm wake mixing strategies. Renewable Energy, 194, 582–595. https://doi.org/10.1016/j.renene.2022.05.110

Gaertner, E., Rinker, J., Sethuraman, L., Zahle, F., Anderson, B., Barter, G., Abbas, N., Meng, F., Bortolotti, P., Skrzypinski, W., Scott, G., Feil, R., Bredmose, H., Dykes, K., Shields, M., Allen, C., & Viselli, A. (2020). Definition of the iea wind 15-megawatt offshore reference wind turbine technical report. www.nrel.gov/publications.

Glauert, H. (1935). Airplane propellers. In Aerodynamic theory: A general review of progress under a grant of the guggenheim fund for the promotion of aeronautics (pp. 169–360). Springer Berlin Heidelberg. https://doi.org/10.1007/978-3-642-91487-4_3

Gutknecht, J., Taschner, E., Viré, A., & van Wingerden, J. (2023). The physical mechanisms behind wake mixing enhancement with dynamic individual pitch control. NAWEA WindTech Conference.

GWEC. (2023). Global wind report 2023. www.gwec.net

Hansen, K. S., Barthelmie, R. J., Jensen, L. E., & Sommer, A. (2012). The impact of turbulence intensity and atmospheric stability on power deficits due to wind turbine wakes at horns rev wind farm. Wind Energy, 15, 183–196. https://doi.org/10.1002/we.512

Heus, T., Jonker, H. J. J., Siebesma, A. P., Heus, T., Heerwaarden, C. C. V., Jonker, H. J. J., Siebesma, A. P., Axelsen, S., Dries, K. V. D., Geoffroy, O., Moene, A. F., Pino, D., Roode, S. R. D., & Arellano, J. V. A.-G. D. (2010). Formulation of and numerical studies with the dutch atmospheric large-eddy simulation (dales) the dutch atmospheric les geoscientific model development discussions formulation of and numerical studies with the dutch atmospheric large-eddy simulation (dales) the dutch atmospheric les. 3, 99–180. https://doi.org/10.5194/gmdd-3-99-2010

Howland, M. F., Bossuyt, J., Martínez-Tossas, L. A., Meyers, J., & Meneveau, C. (2016). Wake structure in actuator disk models of wind turbines in yaw under uniform inflow conditions. Journal of Renewable and Sustainable Energy, 8. https://doi.org/10.1063/1.4955091

IEA. (2022). United states - countries and regions. https://www.iea.org/countries/united-states

IEAWindTask. (n.d.). Iea-15-240-rwt/documentation at master · ieawindtask37/iea-15-240-rwt. https://github.com/IEAWindTask37/IEA-15-240-RWT/tree/master/Documentation

Ivanell, S., Sørensen, J. N., Mikkelsen, R., & Henningson, D. (2009). Analysis of numerically generated wake structures. Wind Energy, 12(1), 63–80. https://doi.org/https://doi.org/10.1002/we.285

Jimenez, A., Crespo, A., Migoya, E., & Garcia, J. (2007). Advances in large-eddy simulation of a wind turbine wake. Journal of Physics: Conference Series, 75. https://doi.org/10.1088/1742-6596/75/1/012041

Jonkman, J. (2013). The new modularization framework for the fast wind turbine cae tool. In 51st aiaa aerospace sciences meeting including the new horizons forum and aerospace exposition. https://doi.org/10.2514/6.2013-202

Kheirabadi, A. C., & Nagamune, R. (2019). A quantitative review of wind farm control with the objective of wind farm power maximization. Journal of Wind Engineering and Industrial Aerodynamics. https://api.semanticscholar.org/CorpusID:199087027

Kimura, K., Iida, M., Tanabe, Y., & Matsuo, Y. (2019). Forced wake meandering for rapid recovery of velocity deficits in a wind turbine wake. AIAA Scitech 2019 Forum. https://doi.org/10.2514/6.2019-2083

Korb, H., Asmuth, H., & Ivanell, S. (2023). The characteristics of helically deflected wind turbine wakes. Journal of Fluid Mechanics, 965. https://doi.org/\doi{10.1017/jfm.2023.390}

Larsen, G. C. (1988). General rights a simple wake calculation procedure.

Lignarolo, L. E., Ragni, D., Ferreira, C. J. S., & van Bussel, G. J. (2014). Experimental quantification of the entrainment of kinetic energy and production of turbulence in the wake of a wind turbine with particle image velocimetry. 32nd ASME Wind Energy Symposium. https://doi.org/10.2514/6.2014-0706

Manwell, J. F., McGowan, J. G., & Rogers, A. L. (2010). Wind energy explained: Theory, design and application.

Martínez, L. A., Leonardi, S., Churchfield, M. J., & Moriarty, P. J. (2012). A comparison of actuator disk and actuator line wind turbine models and best practices for their use. 50th AIAA Aerospace Sciences Meeting Including the New Horizons Forum and Aerospace Exposition. https://doi.org/10.2514/6.2012-900

Meyers, J., Bottasso, C., Dykes, K., Fleming, P., Gebraad, P., Giebel, G., Göçmen, T., & van Wingerden, J.-W. (2022). Wind farm flow control: Prospects and challenges. Wind Energy Science, 7(6), 2271–2306. https://doi.org/10.5194/wes-7-2271-2022

Meyers, J., & Meneveau, C. (2010). Large eddy simulations of large wind-turbine arrays in the atmospheric boundary layer. 48th AIAA Aerospace Sciences Meeting Including the New Horizons Forum and Aerospace Exposition. https://doi.org/10.2514/6.2010-827

Moens, M., Duponcheel, M., Winckelmans, G., & Chatelain, P. (2018). An actuator disk method with tip-loss correction based on local effective upstream velocities. Wind Energy, 21, 766–782. https://doi.org/10.1002/we.2192

Munters, W., Meneveau, C., & Meyers, J. (2016). Turbulent inflow precursor method with time-varying direction for large-eddy simulations and applications to wind farms. Boundary-Layer Meteorology, 159, 305–328. https://doi.org/10.1007/s10546-016-0127-z

Munters, W., & Meyers, J. (2016). Effect of wind turbine response time on optimal dynamic induction control of wind farms. Journal of Physics: Conference Series, 753. https://doi.org/10.1088/1742-6596/753/5/052007

Munters, W., & Meyers, J. (2018). Towards practical dynamic induction control of wind farms: Analysis of optimally controlled wind-farm boundary layers and sinusoidal induction control of first-row turbines. Wind Energy Science, 3, 409–425. https://doi.org/10.5194/wes-3-409-2018

Muscari, C., Schito, P., Viré, A., Zasso, A., Hoek, D. V. D., & Wingerden, J. W. V. (2022). Physics informed dmd for periodic dynamic induction control of wind farms. Journal of Physics: Conference Series, 2265. https://doi.org/10.1088/1742-6596/2265/2/022057

Nilsson, K., Ivanell, S., Hansen, K. S., Mikkelsen, R., Sørensen, J. N., Breton, S.-P., & Henningson, D. (2015). Large-eddy simulations of the lillgrund wind farm. Wind Energy, 18(3), 449–467. https://doi.org/https://doi.org/10.1002/we.1707

Novaes Menezes, E. J., Araújo, A. M., & Bouchonneau da Silva, N. S. (2018). A review on wind turbine control and its associated methods. Journal of Cleaner Production, 174, 945–953. https://doi.org/https://doi.org/10.1016/j.jclepro.2017.10.297

OpenFAST. (n.d.). GitHub - OpenFAST/openfast at v3.4.1. https://github.com/OpenFAST/openfast/tree/v3.4.1

Pirrung, G. R., & van der Laan, M. P. (2018). A simple improvement of a tip loss model for actuator disc and actuator line simulations. https://doi.org/10.5194/wes-2018-59

Prandtl, L. (1921). Applications of modern hydrodynamics to aeronautics.

Quon, E. W., Doubrawa, P., & Debnath, M. (2020). Comparison of rotor wake identification and characterization methods for the analysis of wake dynamics and evolution. Journal of Physics: Conference Series, 1452. https://doi.org/10.1088/1742-6596/1452/1/012070

Réthoré, P.-E., van der Laan, P., Troldborg, N., Zahle, F., & Sørensen, N. N. (2014). Verification and validation of an actuator disc model. Wind Energy, 17(6), 919–937. https://doi.org/https://doi.org/10.1002/we.1607

Schalkwijk, J., Jonker, H. J., Siebesma, A. P., & Meijgaard, E. V. (2015). Weather forecasting using gpu-based large-eddy simulations. Bulletin of the American Meteorological Society, 96, 715–723. https://doi.org/10.1175/BAMS-D-14-00114.1

Shen, W. Z., Mikkelsen, R., Sørensen, J. N., & Bak, C. (2005). Tip loss corrections for wind turbine computations. Wind Energy, 8(4), 457–475. https://doi.org/https://doi.org/10.1002/we.153

Simisiroglou, N., Breton, S. P., & Ivanell, S. (2017). Validation of the actuator disc approach using small-scale model wind turbines. Wind Energy Science, 2, 587–601. https://doi.org/10.5194/wes-2-587-2017

Smagorinsky, J. (1963). General circulation experiments with the primitive equations: I. the basic experiment. Monthly Weather Review, 91(3), 99–164. https://doi.org/10.1175/1520-0493(1963)091<0099:GCEWTP>2.3.CO;2

Sørensen, J. N., & Shen, W. Z. (2002). Numerical Modeling of Wind Turbine Wakes. Journal of Fluids Engineering, 124(2), 393–399. https://doi.org/10.1115/1.1471361

Stevens, R. J., Graham, J., & Meneveau, C. (2014). A concurrent precursor inflow method for large eddy simulations and applications to finite length wind farms. Renewable Energy, 68, 46–50. https://doi.org/10.1016/j.renene.2014.01.024

Stevens, R. J., Martínez-Tossas, L. A., & Meneveau, C. (2018). Comparison of wind farm large eddy simulations using actuator disk and actuator line models with wind tunnel experiments. Renewable Energy, 116, 470–478. https://doi.org/10.1016/j.renene.2017.08.072

Stevens, R. J., & Meneveau, C. (2017, January). Flow structure and turbulence in wind farms. https://doi.org/10.1146/annurev-fluid-010816-060206

Taschner, E., Vondelen, A. A. V., Verzijlbergh, R., & Wingerden, J. W. V. (2023). On the performance of the helix wind farm control approach in the conventionally neutral atmospheric boundary layer. Journal of Physics: Conference Series, 2505. https://doi.org/10.1088/1742-6596/2505/1/012006

Taschner, E., Folkersma, M., Martínez-Tossas, L. A., Verzijlbergh, R., & van Wingerden, J. W. (2023). A new coupling of a gpu-resident large-eddy simulation code with a multiphysics wind turbine simulation tool. Wind Energy. https://doi.org/10.1002/we.2844

Tennekes, H., & Lumley, J. (1972). A first course in turbulence.

Thomsen, K., & Sørensen, P. (1999). Fatigue loads for wind turbines operating in wakes.

Troldborg, N. (2009). Actuator line modeling of wind turbine wakes.

Troldborg, N., Sørensen, J. N., & Mikkelsen, R. (2007). Actuator line simulation of wake of wind turbine operating in turbulent inflow. Journal of Physics: Conference Series, 75. https://doi.org/10.1088/1742-6596/75/1/012063

van der Hoek, D., den Abbeele, B. V., Ferreira, C. S., & van Wingerden, J.-W. (2023). Maximizing wind farm power output with the helix approach – experimental validation and wake analysis using tomographic piv. %5Curl%7Bhttp://arxiv.org/abs/2306.12849%7D

van Dorp. (2016). Large-eddy simulation of wind farms in clear and cloud-topped boundary layers.

Vermeer, L. J., Sørensen, J. N., & Crespo, A. (2003). Wind turbine wake aerodynamics. https://doi.org/10.1016/S0376-0421(03)00078-2

Vondelen, A. A. V., Navalkar, S. T., Kerssemakers, D. R., & Wingerden, J. W. V. (2023). Enhanced wake mixing in wind farms using the helix approach: A loads sensitivity study. Proceedings of the American Control Conference, 2023-May, 831–836. https://doi.org/10.23919/ACC55779.2023.10155965

Wu, Y. T., & Porté-Agel, F. (2011). Large-eddy simulation of wind-turbine wakes: Evaluation of turbine parametrisations. Boundary-Layer Meteorology, 138, 345–366. https://doi.org/10.1007/s10546-010-9569-x

WWEA. (2023). Half-year report 2023, additional momentum for windpower in 2023. www.wwindea.org

A

Description of the HPK input profiles

Here the exact shape of the chord and lift slope profiles are discussed. The continuous profiles are generated by fitting polynomials to the discrete data available in Gaertner et al. (2020). We define:

$$c'(r') = \sum_{i=0}^{10} \max(0, a_i r'^i) \tag{A.1}$$

$$C_{L\alpha}(r') = \sum_{i=0}^{16} \max(0, b_i r'^i) \tag{A.2}$$

The corresponding coefficients are listed in Table A.1. The profiles are plotted in Figure 4.2

Table A.1: Polynomial coefficients of the radial chord and lift slope distributions.

a_0	0.04328217452656468
a_1	0.02711901967475417
a_2	-1.0390679891757433
a_3	20.854446307980812
a_4	-162.4287463301904
a_5	648.3364964791548
a_6	-1513.2595662995625
a_7	2160.622263414656
a_8	-1864.0011715205899
a_9	894.3065839659893
a_{10}	-183.46247119071725

b_0	0.0016708252585269166
b_1	-1.0027335139783622
b_2	40.019296903504475
b_3	-263.60085439185355
b_4	-2.931091788704249
b_5	8104.119649448721
b_6	-46961.602171136685
b_7	136198.73864427223
b_8	-223815.72168216368
b_9	181787.26648218549
b_{10}	6022.012011458497
b_{11}	-123557.1539166327
b_{12}	9587.905441942225
b_{13}	167449.39689163544
b_{14}	-183704.49607207422
b_{15}	83978.56479480717
b_{16}	-14861.39639251259

B

Rotor performance of the IEA 15MW reference turbine

This Appendix contains the rotor performance table used for turbulent simulations (IEAWindTask, n.d.).

Table Part 1

u_∞ [m/s]	C_T [-]	C_P [-]	Ω [rpm]
3.00	0.8030	0.0593	5.00
3.54	0.7897	0.2451	5.00
4.06	0.7845	0.3384	5.00
4.55	0.7872	0.3892	5.00
5.00	0.7884	0.4186	5.00
5.42	0.7819	0.4363	5.00
5.80	0.7925	0.4473	5.00
6.15	0.7839	0.4542	5.00
6.46	0.7882	0.4586	5.00
6.73	0.7848	0.4615	5.00
6.96	0.7802	0.4632	5.00
7.15	0.7799	0.4636	5.08
7.31	0.7799	0.4636	5.19
7.42	0.7799	0.4636	5.27
7.50	0.7799	0.4636	5.32
7.53	0.7799	0.4636	5.35
7.54	0.7799	0.4636	5.35
7.58	0.7799	0.4636	5.39
7.67	0.7799	0.4636	5.45
7.80	0.7799	0.4636	5.54
7.97	0.7799	0.4636	5.66
8.17	0.7799	0.4636	5.80
8.42	0.7799	0.4636	5.98
8.70	0.7799	0.4636	6.18
9.02	0.7799	0.4636	6.41

Table Part 2

u_∞ [m/s]	C_T [-]	C_P [-]	Ω [rpm]
9.38	0.7799	0.4636	6.66
9.78	0.7799	0.4636	6.94
10.20	0.7799	0.4636	7.25
10.65	0.7720	0.4638	7.50
10.67	0.7463	0.4618	7.50
11.17	0.5657	0.4029	7.50
11.69	0.4677	0.3507	7.50
12.25	0.3818	0.3048	7.50
12.84	0.3285	0.2648	7.50
13.46	0.2871	0.2300	7.50
14.10	0.2445	0.1999	7.50
14.77	0.2074	0.1740	7.50
15.47	0.1868	0.1516	7.50
16.18	0.1535	0.1324	7.50
16.92	0.1329	0.1159	7.50
17.67	0.1279	0.1017	7.50
18.44	0.1027	0.0894	7.50
19.23	0.0942	0.0789	7.50
20.02	0.0837	0.0698	7.50
20.84	0.0757	0.0620	7.50
21.66	0.0666	0.0552	7.50
22.48	0.0595	0.0493	7.50
23.32	0.0537	0.0442	7.50
24.16	0.0487	0.0398	7.50
25.00	0.0443	0.0359	7.50

C

Boundary layer development in the wind farm domain

Here the development of turbulence intensity (TI) and free-stream velocity (u_∞) will be shown for the simulation setup listed in Section 6.1. The results are shown in Figure C.1. The TI and u_∞ development over time is determined by running an empty simulation, i.e. the domain without turbines, and tracking its average value at hub height where the six turbines of the first row would be positioned (i.e. x = 2.168 km). All values shown are 10 minute averages, where the x-axis shows the averaging time intervals. This means that time averaging interval 0 corresponds to the average over the domain 0-10 min, interval 1 corresponds to 10-20 min and so on.

For investigating the wind farm performance, it is decided to remove the transient where turbulence is still developing from the averaging period. Based on Figure C.1 it is decided to average farm results over the interval 14 until 31, i.e. from minute 140 to 320.

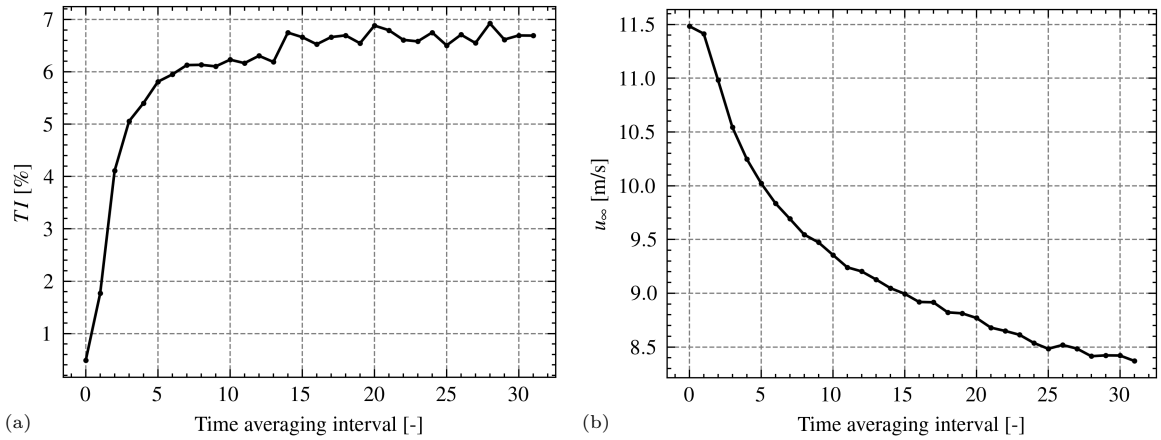

Figure C.1: The development of turbulence intensity (a) and free-stream velocity (b) over time for the wind farm simulation setup. The figures contain 10-minute averaged values, where the averaging intervals are shown on the x-axis.